Politecnico di Torino

Politecnico di Torino

Sustainable nuclear energy

A.a. 2025/2026

Graduation Session Luglio 2026

PIC simulation of laser-plasma interaction in sub-critical foams

Relatori:

Roberto Bonifetto
Antonio Froio
Raffaella Testoni
Antonio Zurzolo

Candidato:

Lorenzo Giurdanella

Summary

Interactions between laser and plasma have been drawing attention due to their various applications, from the production of energy by inertial confinement fusion to the acceleration of particles. The focus is maximizing the absorption of energy from the laser by the target. A promising solution for that is the use of foams.

Foams are porous solids that have been shown to perform better than other solutions in terms of deposition of energy from the interaction with a laser. Despite this, interactions with such a medium are yet to be fully understood, and work is being carried out to improve their knowledge also thanks to more accurate and reliable models. The goal of the present thesis is to study how foams interact with laser pulses at a microscopic level, considering a single foam elemental unit; in particular, the main interest of this work is the dependence of the physical phenomena governing the energy absorption on the foam parameters.

First, the general plasma behavior is presented, highlighting its main features and the key parameters needed to describe it. Then, a mathematical description of its interactions with incoming electromagnetic waves is provided.

The numerical simulations are carried out using SMILEI, a particle-in-cell code for kinetic simulations of plasmas. Therefore, the main workflow of this kind of codes is presented, as well as the specific features of SMILEI.

The code is first used for the reproduction of results from the literature, which will then serve as a basis to compare results from other simulations. Scenarios with variations in the foam-element parameters, such as its dimensions, will be explored to investigate how the characteristics of the foam influence the different mechanisms of absorption and which of them dominates.

Table of Contents

Chapter 1

Laser-plasma interaction in nano-foams

Plasma description is fundamental in a wide range of fields, from astrophysics to industrial applications. Among the latter, several have drawn the attention to the study of nano-foams and the modelling of their interaction with laser pulses aimed at the production of plasma.

In this chapter an introduction to plasma is presented, giving a physical description and presenting the most relevant parameters and phenomena that characterize it. Despite being a general description, understanding the basic mechanisms of plasma evolution is fundamental to then study its interactions with electromagnetic waves.

Once basic concepts will have been presented, the following section describes in more detail how plasma interacts with laser, and in particular the physical mechanisms underlying energy absorption by particles. Additionally, a description of the Mie theory of scattering is provided as a mathematical model to quantify absorption and its distribution over the target.

1.1 Introduction to plasma physics

Sometimes plasma is referred to as an ionized gas. Though not being completely wrong, such a description might be reductive and misleading. Plasma is characterized by a series of phenomena that are not present in gases, and therefore require an adequate description. Indeed, plasma is a different state of matter (often called as the "fourth state of matter"). A more rigorous definition is that of a quasi-neutral gas of charged particles showing collective behaviour [1]. Given the definition, the problem of describing what a plasma is shifts to explaining what is meant by "quasi-neutrality" and "collective behaviour".

The first point to highlight is the "quasi neutrality". A plasma can be produced by the ionization of a gas, and is made of positively charged particles, ions, and electrons. In this case, if the gas is originally made of neutral atoms with atomic number Z, Z will also be the number of electrons per atom, and, when completely ionized, it will also be the ration between the number density of electrons and the number density of ions, with the number density being the number of ions of a given species per unit volume, usually expressed as cm^{-3}. Despite being made of charged particles, plasma is neutral on a larger scale. Calling the number density of ions and electrons n_i and n_e, respectively, the net charge can be expressed as:

$$n_q = n_i q_i - n_e q_e. \tag{1.1}$$

The electric charge of an electron is $q_e = -e$, while of an ion it's $q_i = Z_e$. Since, as explained above, the ratio between the number densities is $\frac{n_e}{n_i} = Z$, for a sufficiently large volume:

$$n_q \approx \frac{n_e}{Z} Ze - n_e e = 0. \tag{1.2}$$

The second main property defining a plasma is the exhibition of a collective behaviour. To better understand this concept, it is useful to make a comparison: although a certain degree of ionization is possible, gas particles are usually neutral; therefore, there is no net electromagnetic force acting on it and collisions is the main driver of interaction between gas particles and of the transmission of macroscopic forces acting on them. Instead, for a plasma, since the particles are charged, the creation of local accumulation of charges is possible, with a consequent formation of an electric field and a charge current. If we consider two charged regions whose distance is r, the force exchanged between them scales as $1/r^2$; however, for a given solid angle, the volume of plasma that can affect a region increases as r^3 [2]. For this reason long-range interactions play a fundamental role in plasmas, to the point that, in some cases, collisions can be neglected (we refer to these cases as collision-less plasma).

After explaining what a plasma is, some key parameters need to be presented to understand its properties. A fundamental concept in plasma physics is Debye shielding [3]. Let us consider a voltage applied to a plasma As a consequence, an electric field will be produced, and charged particles will move according to the sign of their charge: positive ones toward the negative pole and, conversely, negative ones toward the positive one. Two layers are then formed at the extremities, with accumulations of charges that create an electric field whose direction is opposite to the one arising from the applied voltage. This phenomenon is the Debye shielding. Since the layers of particles have a finite thickness, the shielding is not perfect. Assuming, for simplicity, a 1D geometry, the electric potential distribution ϕ follows the equation:

$$\frac{d^2\phi}{dx^2} - \frac{e^2 n_0}{\epsilon_0 k_B}\left(\frac{1}{T_e} + \frac{1}{T_i}\right)\phi = 0, \tag{1.3}$$

where ϵ_0 is the void dielectric constant, k_B is the Boltzmann constant, T_e is the electron temperature, T_i the ion temperature and e is the charge of the electron.

From this equation it is possible to define the Debye length:

$$\frac{1}{\lambda_D^2} = \frac{1}{\lambda_{De}^2} + \frac{1}{\lambda_{Di}^2} = \frac{e^2 n_0}{\epsilon_0 k_B T_e} + \frac{e^2 n_0}{\epsilon_0 k_B T_i} \tag{1.4}$$

which is a quantification of the penetration length. The solution to equation 1.3 goes down to zero in a length around λ_D, as depicted in figure 1.1. This solution is valid for a macroscopic dimension of plasma $L >> \lambda_D$.

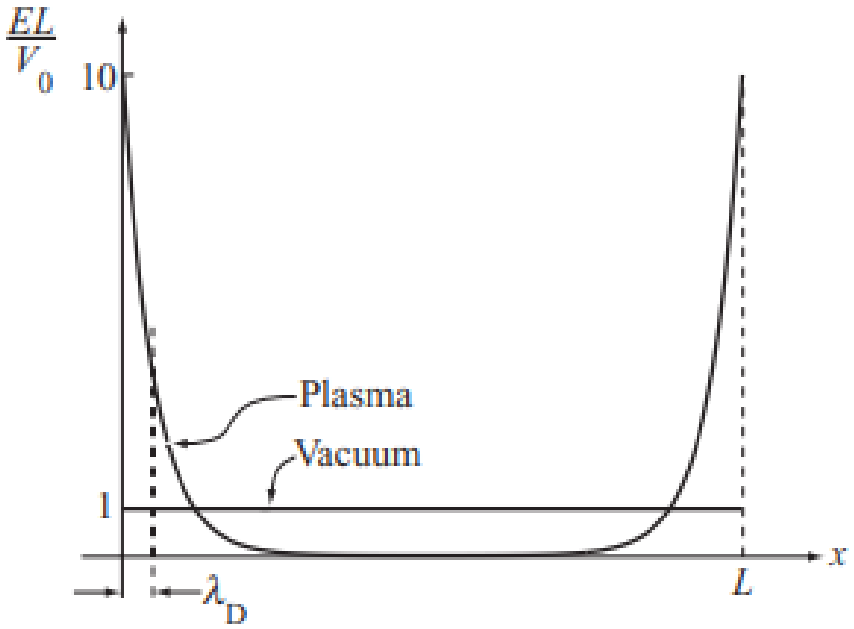

Figure 1.1: Representation of the shielding of a plasma from an external voltage. The electric potential drops significantly at a distance of around one Debye length from the extremities [3].

In literature the Debye length is often identified as λ_{De}; this approximation is valid for $T_i >> T_e$. In many cases $T_i \approx T_e$, and neglecting the contribution λ_{Di} leads to an increase of Debye length by a factor in the order of unity. If only an estimation of its value is needed, this approximation is valid.

Debye shielding is also linked to quasi-neutrality. Although one might expect that the effect of the Coulomb force of a charge particle might extend indefinitely,

its range is actually limited by the other particles that surround it; the extent of this range is quantified by the Debye length [4].

From the Debye length it is possible to define the plasma parameter, which is a measure of the long-range collective effects over short range ones (i.e. collisions) [3]. It is expressed as the number of electrons contained in the volume of a sphere whose radius is λ_D :

$$\Lambda_D = \frac{4\pi}{3} n_e \lambda_D^3. \tag{1.5}$$

A third fundamental quantity, fundamental for the description of a plasma, is plasma frequency, defined as:

$$\omega_p = \sqrt{\frac{e^2 n_e}{\epsilon_0 m_e}}. \tag{1.6}$$

Plasma frequency is a measure of how fast electrons respond to external fields. Being much lighter than ions, their response is faster, but still finite. A comparison of macroscopic time scales and frequencies with ω_p shows if electrons have enough time to complete their motion and shield out the field.

In light of the parameters listed above, an ionized gas behaves like a plasma (i.e. shows quasi-neutrality and collective behaviour) if the following conditions are fulfilled [3]:

- $\lambda_D << L$, where L is the macroscopic characteristic length of the plasma. This condition guarantees shielding from DC external electric fields
- $\omega_p >> v_{Te}/L$, with v_{Te} being the thermal velocity of electrons. This condition guarantees shielding from AC external electric fields
- $\Lambda_D >> 1$, which ensures the prevalence of long-range collective interactions over collisions.

1.2 Laser-matter interaction and plasma production

Several techniques for the production of plasma exist, differing in the physical processes they rely on (e.g. thermal process, use of beam particles, application of external voltage, etc.) [5]. However, all these methods boil down to the same principle, the ionization of atoms. Electrons are bound to the nucleus of an atom through electrostatic force. To ionize atoms energy has to be transferred to electrons to overcome the force that binds them to nuclei, and a certain threshold must be exceeded; this threshold is called ionization energy. This threshold becomes higher

and higher as more electrons are ionized from a given atom. As a result, great amounts of energy are required for the complete ionization of atoms and, therefore, the production of plasma. Several traditional techniques rely on gaseous targets, inducing collisions between atoms and, consequently, ionization. However, over time, an interest has been raised in the use of solid targets, coupled with lasers as energy sources.

The word laser is an acronym that stands for Light Amplification by Stimulated Emission of Radiation. Laser beams are electromagnetic waves just like normal light, but it exhibits several properties that make it different from other light sources [6], such as monochromaticity (consisting of one wavelength) and high directionality. An additional, fundamental property of laser beams is coherence, both spatial and temporal. Spatial coherence implies that the phase difference between two points remains constant in time, while temporal coherence implies that, for two time instants t_1 and $t_1 + \tau$ separated by a fixed time interval, the phase difference of the electric field at a point P between the two time instants is the same for any t_1.

Using lasers as energy source allows to transfer large amounts of energy in very short time scales, from nanoseconds to femtoseconds, and focusing the interaction is a localized portion of space. Intensities can reach values ranging from 10^{14} to $10^{18} W/m^2$, making them the only viable option for applications such inertial confinement fusion.

As mentioned above, the process of plasma formation takes place when electrons gain enough energy to overcome the potential that binds it to the atom. Absorption of energy by electrons can take place thanks to different physical processes, depending on several laser and target atom parameters. To understand these process, we first introduce the so-called Keldysh parameter [7]:

$$\gamma = \omega \frac{\sqrt{2mI_0}}{2eE_0}, \tag{1.7}$$

where I_0 is the intensity of the laser, ω its frequency and E_0 is the electric field intensity. The value of the Keldysh parameter allows to distinguish between two different regimes, dominated by different ionization phenomena [8].

For $\gamma >> 1$ multi-photon ionization takes place. From quantum mechanics it is know that light has a double nature, a wave-like one and a particle-like one. The particles making up light are photons; interaction of electromagnetic waves with matter can be also thought as interaction of photons with atoms. Each photon carries an energy that is expressed by:

$$E_\gamma = h\nu, \tag{1.8}$$

where h is the Planck constant and ν is the frequency of light. A photon, and the energy it carries, can be absorbed by an electron, which is in turn excited.

The electron is ionized only if the energy carried by the photon is larger than the ionization energy, otherwise it is only excited to a higher bound state. However, more than one photon can be absorbed simultaneously and their combined energy can overcome the binding potential: this phenomenon is called multi-photon ionization.

When $\gamma << 1$, the intensity of the electric field becomes more relevant and quantum effects play a fundamental role. The presence of the electric field of the laser can distort the Coulomb potential making it narrower; in this way the energy required by the electron to move from bound to free state is lower and can escape by quantum tunnelling.

If the electric field intensity further increases, the suppression of the potential barrier is such that the ionization energy falls below the state energy of the electron. This case is referred to as over-barrier ionization (OBI). An estimation of the threshold for the electric field to have OBI is:

$$E_{OBI} = \frac{I_p^2}{4Z}, \tag{1.9}$$

where I_p is the ionization potential and Z the charge of the residual ion. This formula is retrieved for a very simplified case of electrons moving a 1D cartesian geometry. A more detailed treatment of tunnel ionization and OBI can be found in [9].

Once electrons move to a free state, these can still absorb energy from light thanks to inverse bremsstrahlung: when a free electron moves close to an ion, it can absorb a photon and its energy, and as a results speeds up or changes direction. In their motion electrons can collide with neutral or partially ionized atoms, making in this way ionization process also collisional. Furthermore, these collisions can take place also with completely ionized atoms, transferring to them energy. This is therefore the mechanism of heating up of ion species in plasma.

At this point it's fundamental to introduce the concept of critical density. Considering an electromagnetic wave with travelling in a plasma, the dispersion relation for its propagation can be written as [2]:

$$\omega^2 = \omega_p^2 + c^2 k^2, \tag{1.10}$$

where ω_p is the plasma frequency and ω and k are the frequency and the wave number of the electromagnetic wave. If the beam has a frequency ω the relation will yield a value for k. However, the relation shows a cut-off: for a certain value of the frequency, $k = 0$, and for values beyond that no real k can satisfy the relation. The cut-off is for $\omega = \omega_p$, and this condition is satisfied for an electron frequency

$$n_c = \frac{m\epsilon_0\omega^2}{e^2}, \tag{1.11}$$

called the critical frequency. For $n_e > n_c$ plasma becomes opaque to laser and waves are reflected.

When a laser beam hits a solid target, atoms start to ionize and the irradiated portion turns into a plasma. Due to the high density of solids, the resulting plasma is overcritical (density higher than the critical one) and therefore prevents the beam to further propagate through the target. As a result, a large part of the incoming energy is reflected, and a large part of the target is converted to plasma by conduction, which is an inefficient way to absorption. With the aim of improving the efficiency of this process, a viable path is employing nanofoams [10].

Nanofoams are porous, nanostructured materials with a very large fraction of sub-micrometric voids and a disordered, fractal-like backbone of nanoparticles. [11]. In the context of laser-matter interaction foams find application thanks to the large fraction of void surrounding the solid parts, and therefore lower density than normal solid targets. The difference in using a porous material rather than a normal solid lies in the first stage of the process. The porous structure allows the penetration of the incoming electromagnetic wave up to a longer distance, called transparency length. The structures making up the foam are ionized and turned into plasma; the plasma elements, being surrounded by void, expand due to their pressure and fill the pores. Foams are characterized by a value of final number density, at the end of the process of plasma formation and homogenization, that can be higher or lower than the critical one, and are therefore called over-critical and sub-critical foams, respectively. In the case of sub-critical foams, the final plasma is transparent to light and therefore laser absorption takes place. Near-critical foams have proven to yield a better absorption than normal solid targets [12] and the absorption efficiency can reach 80 to 90 percentage for overcritical foams [13].

So far literature has mostly focused on modelling of foams interaction with laser on a macroscopic level. Instead, in what follows, the attention is shifted on a microscopic treatment of foams, focusing on the evolution of a single element evolution in its interaction when hit by a laser beam. In the next section the mathematical framework that describes the incidence of electromagnetic waves on a target with the dimensions of interest is presented.

1.3 Mie scattering on cylindrical target

To better describe a laser beam's interaction with foams on a macroscopic level, it is fundamental to first understand how absorption takes place for a single foam structural element, and to tackle this problem Mie theory of scattering is presented.

Mie theory is a particular solution of Maxwell's equations for a plane electromagnetic wave scattering over a spherical particle whose dimension is comparable to the wavelength. A solution to the same problem for particles much smaller or much

larger than the wavelength was already obtained thanks to Rayleigh scattering and Rayleigh-Gans-Debye scattering, respectively. Mie theory allowed to bridge the two, allowing calculation for particles of any size [14].

The aim of this section is providing an overview of Mie scattering, highlighting the main mathematical backbone of the theory, with a focus on the results for scattered and absorbed power distributions and their dependence on some physical parameters. Despite considering a spherical particle as a target, Mie theory can be applied similarly to a cylindrical one. The treatment here proposed is based on the work in [15]; mathematical passages are only detailed, living the above-mentioned work as a reference for a more complete discussion.

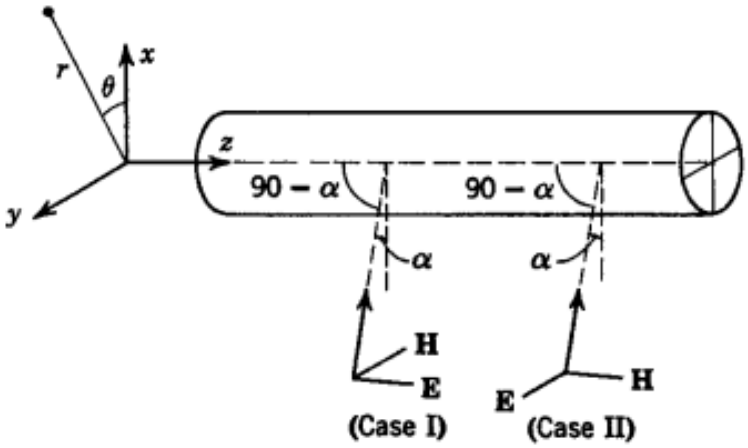

Figure 1.2: Representation of an electromagnetic wave on a cylindrical target [15].

Figure 1.2 shows the geometry of the problem. z-axis is directed along the axis of the cylinder, while its base is parallel to the x-y plane. Two different cases are depicted, differing in the orientation of the fields; these two cases are analysed later on. The laser propagates defining an incidence angle α with the perpendicular to the cylinder.

Cylindrical geometry is adopted and quantities are therefore expressed in function of coordinates r, θ and z, with r and θ such that $x = rcos\theta$ and $y = rsin\theta$. The problem requires the solution of Maxwell's equations, in particular Ampere-Maxwell law and and Maxwell-Faraday law, which are here written adopting Gaussian units:

$$\nabla \times \mathbf{H} = \frac{1}{c}(4\pi\mathbf{J} + \frac{d}{dt}\mathbf{D}), \tag{1.12}$$

$$\nabla \times \mathbf{E} = -\frac{1}{c}\frac{d}{dt}\mathbf{H}, \tag{1.13}$$

where $\mathbf{H}$ is the magnetic field strength, $\mathbf{J} = \sigma\mathbf{E}$ is the current density, $\mathbf{D} = \epsilon\mathbf{E}$ is the dielectric displacement, σ the electrical conductivity and ϵ the dielectric constant.

The fields are assumed to be oscillating quantities in the form of $\mathbf{A} \propto e^{i\omega t}$, with ω being the frequency of the wave. Applying the temporal derivative operators, the above equations can be written as:

$$\nabla \times \mathbf{H} = \mathbf{ikm^2E}, \tag{1.14}$$

$$\nabla \times \mathbf{E} = -ik\mathbf{H}, \tag{1.15}$$

where k is the wavenumber and m, defined as $m^2 = \epsilon - \frac{4\pi i\sigma}{\omega}$, is the complex refractive index of the medium.

By virtue of the two equations above, it is possible to show that the field $\mathbf{H}$ and $\mathbf{E}$ need to satisfy the equation:

$$\nabla^2\mathbf{A} + k^2m^2\mathbf{A} = 0. \tag{1.16}$$

Elementary solutions to this equation can be found from the following theorem: if ψ is a solution to the equation:

$$\nabla^2\psi + k^2m^2\psi = 0, \tag{1.17}$$

it is possible to define the two following vector quantities:

$$\mathbf{M}_\psi = \nabla \times (\mathbf{z}\psi), \tag{1.18}$$

$$mk\mathbf{N}_\psi = \nabla \times \mathbf{M}_\psi, \tag{1.19}$$

which are related between themselves by:

$$mk\mathbf{M}_\psi = \nabla \times \mathbf{N}_\psi; \tag{1.20}$$

$\mathbf{H}$ and $\mathbf{E}$ can then be expressed as:

$$\mathbf{E} = \mathbf{M}_v + i\mathbf{N}_u, \tag{1.21}$$

$$\mathbf{H} = m(-\mathbf{M}_u + i\mathbf{N}_v), \tag{1.22}$$

where u and v are solutions to equation 1.17.

We can write a generic plane wave as:

$$\psi_0 = e^{i\omega t - ik(xcos\alpha + zsin\alpha)} \tag{1.23}$$

,

where α is the incidence, and consider two cases:

- Case I: $u = \psi_0$ and $v = 0$, which leads to $E_x = -sin\alpha(ik\psi_0 cos\alpha)$, $E_z = cos\alpha(ik\psi_0 cos\alpha)$ and $H_y = -(ik\psi_0 cos\alpha)$
- Case II: $u = 0$ and $v = \psi_0$, which leads to $H_x = -sin\alpha(ik\psi_0 cos\alpha)$, $H_z = cos\alpha(ik\psi_0 cos\alpha)$ and $E_y = -(ik\psi_0 cos\alpha)$

For the rest of the chapter we are going to consider laser propagating perpendicular to the cylinder, i.e. $\alpha = 0$; in this way the first case corresponds to **E** parallel to z-axis, while the second to the magnetic field parallel to the axes of the cylinder. The function ψ_0 can be expanded in series of Bessel functions of the first kind, yielding, for the electric field in the first case (similarly for the magnetic field for the second on):

$$E_z = e^{-i\omega t} \sum_n J_n(kr) i^n e^{in\theta}. \tag{1.24}$$

As for the boundary conditions, they require that **E** and **H** are continuous at the surface ($r = a$). After some passages it is possible to find expressions for a_n and b_n, which are scattering coefficients. These coefficients are expressed in terms of the Bessel functions J_n, which represent the incoming light, and the Hankel functions of the first kind, $H_n^{(1)}$, which represent the scattered light. The expressions for these coefficients are:

$$a_n = \frac{J_n'(y)J_n(x) - mJ_n(y)J_n'(x)}{J_n'(y)H_n(x) - mJ_n(y)H_n'(x)}, \tag{1.25}$$

$$b_n = \frac{mJ_n'(y)J_n(x) - J_n(y)J_n'(x)}{mJ_n'(y)H_n(x) - J_n(y)H_n'(x)}, \tag{1.26}$$

with $x = ka$ and $y = mka$.

The angular dependence of the scattered light can be expressed by the factors $T_a(\theta)$ and $T_b(\theta)$:

$$T_a(\theta) = \sum_n a_n e^{in\theta}, \tag{1.27}$$

$$T_b(\theta) = \sum_n b_n e^{in\theta}. \tag{1.28}$$

These two factors have a similar meaning to the scattering amplitude function $S(\theta)$ in the case of finite particles, T_b for case I and T_a for case II.

If l is the length of the cylinder, i_0 the intensity of the laser and $|t|^2 = |t_a|^2 + |t_b|^2$, the scattered power is $p_{sca} = \frac{4l}{k} i_0 \overline{|t|}^2$ and the extinction power is $p_{ext} = \frac{4l}{k} i_0 re[t(0)]$. the absorbed power is then easily calculated as $p_{abs} = p_{ext} - p_{sca}$. it is also possible to define the corresponding cross sections, by just dividing the power by the intensity i_0, and the effective factors by dividing the cross section by the geometrical one $\sigma_{geom} = 2al$.

From the theory presented in this section, the dependence of the scattering and absorption on the radius of the cylinder, their angular distribution and the influence of the polarization of the laser can be retrieved. This work is done in [16], where Mie theory is applied to the configurations analysed in the simulations presented by the paper. These results will be discussed in the third section, where the these simulations are reproduced.

Chapter 2

Particle-in-cell codes

Plasmas can be described by means of two main approaches: a simplified one which considers each species of particles as a fluid, and a more general one that allows a description that considers its specific distribution. The latter is the one adopted in particle-in-cell codes. In this chapter the theoretical models on which they are based, as well as their numerical implementation are presented; features specific to SMILEI are described too.

2.1 Introduction to particle-in-cell codes

Plasmas involve high numbers of particles belonging to different species. To each species it is associated a distribution function which contains the information on how the particles are distributed in space and in the velocity phase-space. In the most general case, this function depends on time, space coordinates and velocity:

$$f_s = f_s(t, \mathbf{x}, \mathbf{v}), \tag{2.1}$$

where $\mathbf{x} = (x, y, z)$ denotes the particle's position, $\mathbf{v} = (v_x, v_y, v_z)$ the particle's velocity, and s is a subscript that refers to the species.

Being f_s a function of seven variables, it is not trivial to deal with. To simplify the mathematical modelling, in plasma physics an approximation is made: if the collisions are frequent enough, and if they are not subject to strong external forces, they eventually reach thermodynamic equilibrium and their distribution function is a Maxwellian whose velocity dependence is eliminated. For a Maxwellian distribution the velocity is uniquely specified by the temperature [2], and therefore the dependence of f is only on four variables. In this framework each is species is treated as a fluid characterized by macroscopic quantities integrated over velocity. These fluids are described by a set of equations of motion which are coupled to Maxwell's equations.

When dealing with particles whose distribution is far from equilibrium, this approach in not viable and all dependencies need to be considered. Numerical simulations are then required, and these can be carried out by particle-in-cell (PIC) codes. In what follows the theoretical framework on which PIC codes are based is illustrated.

Let us consider a collisionless plasma made of a certain number of species. For each species s, the distribution function evolves according to the Boltzmann–Vlasov equation [17]:

$$\frac{\partial f_s}{\partial t} + \frac{\mathbf{p}}{m_s \gamma} \nabla f_s + \mathbf{F} \nabla_p f_s = 0, \tag{2.2}$$

where $\mathbf{p}$ is the momentum, m_s is the mass of particles belonging to s, and γ is the Lorentz factor, defined as $\gamma = \sqrt{1 + \frac{\mathbf{p}^2}{m_s c^2}}$, with c being the speed of light in vacuum. $\mathbf{F}$ is the Lorentz force acting on a particle with a velocity $\mathbf{v} = \mathbf{p}/(m_s\gamma)$ and charge q_s:

$$\mathbf{F} = q_s(\mathbf{E} + \mathbf{v} \times \mathbf{B}) \tag{2.3}$$

The Lorentz force arises from collective electric and magnetic fields that satisfy Maxwell's equations:

$$\nabla \cdot \mathbf{E} = \frac{\rho}{\epsilon_0}, \tag{2.4}$$

$$\nabla \cdot \mathbf{B} = 0, \tag{2.5}$$

$$\partial_t \mathbf{B} = -\nabla \times \mathbf{E}, \tag{2.6}$$

$$\partial_t \mathbf{E} = \frac{1}{c^2} \nabla \times \mathbf{B} - \frac{1}{\epsilon_0} \mathbf{J}, \tag{2.7}$$

where ϵ_0 and μ_0 are, respectively, the vacuum permittivity and permeability. The charge density ρ and current density $\mathbf{J}$, appearing in Maxwell's equations, are related to the distribution function according to the following relations:

$$\rho(t, \mathbf{x}) = \sum_s q_s \int d^3 p f_s(t, \mathbf{x}, \mathbf{p}), \tag{2.8}$$

$$\mathbf{J}(t, \mathbf{x}) = \sum_s q_s \int d^3 p \mathbf{v} f_s(t, \mathbf{x}, \mathbf{p}) \tag{2.9}$$

The main idea underlying PIC codes is the discretization of the distribution function as a sum of a certain number N_p of so-called "macro-particles" (also, quasi-particles or super-particles); f_s is then rewritten as:

$$f_s(t, \mathbf{x}, \mathbf{p}) = \sum_p^{N_p} w_p S(\mathbf{x} - \mathbf{x}_p(t))\delta(\mathbf{p} - \mathbf{p}_p(t)), \tag{2.10}$$

where w_p is a weight associated to each macro-particle, $\mathbf{x}_p$ and $\mathbf{p}_p$ are, respectively, the position and momentum of the p macro-particle, $\delta()$ is the Dirac delta distribution and $S(\mathbf{x})$ is a shape function associated to all macro-particles.

By plugging 2.10 in 2.2 the equations of motions satisfied by each macro-particle p are obtained:

$$\frac{d\mathbf{x}_p}{dt} = \frac{\mathbf{u}_p}{\gamma}, \tag{2.11}$$

$$\frac{d\mathbf{u}_p}{dt} = \frac{q_s}{m_s}(\mathbf{E}_p + \frac{\mathbf{u}_p}{\gamma_p} \times \mathbf{B}_p), \tag{2.12}$$

where $\mathbf{E}_p$ and $\mathbf{B}_p$ are the electric and magnetic fields interpolated at the particle position, using the shape function:

$$\mathbf{E}_p = \int d\mathbf{x} S(\mathbf{x} - \mathbf{x}_p)\mathbf{E}(x), \tag{2.13}$$

$$\mathbf{B}_p = \int d\mathbf{x} S(\mathbf{x} - \mathbf{x}_p)\mathbf{B}(x), \tag{2.14}$$

2.2 Numerical implementation

In the previous section the physical models employed by PIC codes were explained. The numerical methods adopted to implement them are discussed in this section: the initalization of particles, the algorithm of the code and discretization methods.

2.2.1 Initialization

The first step of the initialization is loading the macro-particles. Users are required to provide, for each species, the number density n_s and its distribution, the number of macro-particles per cell N_s, as well as the mean velocity $\mathbf{v}_s$ and the temperature T_s. A weight is assigned to each particle; specifically in SMILEI, the weight of a macro-particle is defined as:

$$w_p = \frac{n_s(\mathbf{x}_p(t=0))}{N_s(\mathbf{x}_p(t=0))}, \tag{2.15}$$

and remains the same for the whole simulation. Once all particles are uploaded, initial charge density and current density are projected onto the grid. After this step, Poisson's equation is solved to compute the electric field. Lastly, external

fields can be prescribed, which are then summed to the ones to the ones arising from the charges.

It's useful to highlight that, if the electric charge always satisfies the continuity equation, 2.4 and 2.5 are automatically satisfied if they were satisfied initially [17]. In light of this, only the other two Maxwell equations, the ones describing how the two fields evolve in time, need to be solved.

2.2.2 PIC loop

Once the simulation is completed, the PIC loop is started and performed for a certain number of timesteps N. The loop consists of four steps: interpolation of electric and magnetic fields at particle positions $\mathbf{x}_p$; advance of particles; projection of new charge density and current density; computation of the new electric and magnetic fields. In what follows these passages are detailed for a generic passage from a timestep n to the following one, n+1.

Fields are interpolated at the position of each particle using equations 2.13 and 2.14:

$$\mathbf{E}_p^{(n)} = \int d\mathbf{x} S(\mathbf{x} - \mathbf{x}_p^{(n)}) \mathbf{E}^{(n)}, \tag{2.16}$$

$$\mathbf{B}_p^{(n)} = \int d\mathbf{x} S(\mathbf{x} - \mathbf{x}_p^{(n)}) \mathbf{B}^{(n)} \tag{2.17}$$

As it will be better explained later on, when the solvers for Maxwell's equations will be illustrated, the fields are computed at staggered time instants; more precisely, the electric field at integer time steps, while the electric field at semi-integer ones. Therefore, being $\mathbf{B}$ not available at an integer timestep n, in 2.17 $\mathbf{B}_p^{(n)} = \frac{1}{2}(\mathbf{B}_p^{(n+\frac{1}{2})} + \mathbf{B}_p^{(n-\frac{1}{2})})$ is used.

Fields interpolated at time step n are then used to compute the new positions of macro-particles by using equations 2.11 and 2.12. In order to solve it, a leap-frog integrator is adopted, which is second-order, explicit method. The main scheme adopted in PIC codes is the Boris pusher, which computes the new particle positions and velocities as:

$$\mathbf{u}_p^{(n+\frac{1}{2})} = \mathbf{u}_p^{(n-\frac{1}{2})} + \frac{q_s}{m_s} \Delta t [\mathbf{E}_p^{(n)} + \frac{\mathbf{u}_p^{n+\frac{1}{2}} + \mathbf{u}_p^{n-\frac{1}{2}}}{2\gamma_p^{(n)}} \times \mathbf{B}_p^{(n)}], \tag{2.18}$$

$$\mathbf{x}_p^{(n+1)} = \mathbf{x}_p^{(n)} + \Delta t \frac{\mathbf{u}_p^{(n+\frac{1}{2})}}{\gamma_p^{(n+\frac{1}{2})}} \tag{2.19}$$

It is worth noting the existence of another scheme, the Vay pusher, which also adapts the leap-frog scheme in an alternative way.

After computing the positions of quasi-particles at timestep n+1, charge density and current density at new timestep are updated. For current density this is done by density decomposition method [18], proposed by Eriskepov, which ensures charge conservation. Charge density can be deposited with a similar method. As already mentioned, the use of a method that conserves charge allows to satisfy Gauss equations without solving them.

The last step is then the calculation of the new electric and magnetic fields from 2.6 and 2.7. The approach used to solve them is the finite-difference time-domain (FDTD) method, which employes the Yee grid, a staggered grid, where the fields and charge and current densities are defined at different points. A scheme of Yee grid is shown in figure 2.1. The electric and magnetic fields are computed, respectively, at integer and semi-integer time-steps.

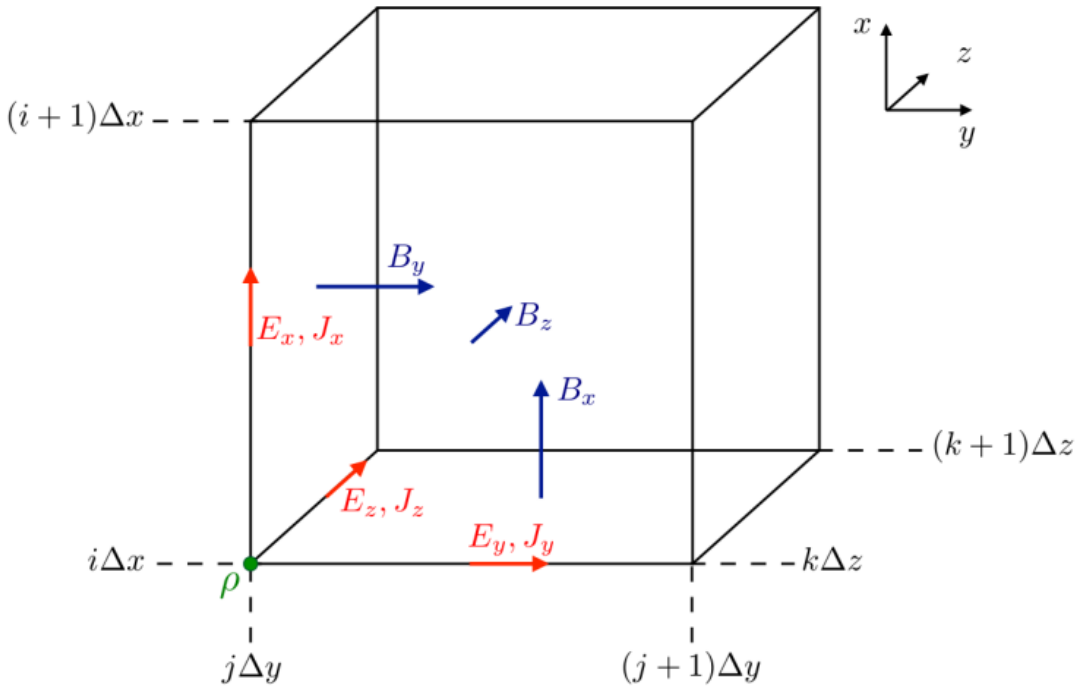

Figure 2.1: Representation of Yee grid

Knowing the current density at n+1, the Maxwell-Ampere equation is solved first:

$$\mathbf{E}^{(n+1)} = \mathbf{E}^n + \Delta t[(\nabla \times \mathbf{B})^{(n+\frac{1}{2})} - \mathbf{J}^{(n+\frac{1}{2})}] \tag{2.20}$$

The electric field at the new timestep is then plugged into the Faraday-Maxwell equation:

$$\mathbf{B}^{(n+\frac{3}{2})} = \mathbf{B}^{(n+\frac{1}{2})} - \Delta t(\nabla \times \mathbf{B})^{(n+1)} \tag{2.21}$$

By way of example, the explicit expression for the x-component of the electric field is here reported:

$$\frac{(E_x)^{(n+1)}_{i+\frac{1}{2},j,k} - (E_x)^{(n)}_{i+\frac{1}{2},j,k}}{\Delta t} = (j_x)^{(n+\frac{1}{2})}_{i+\frac{1}{2},j,k} + (\partial_y B_z)^{(n+\frac{1}{2})}_{i+\frac{1}{2},j,k} - (\partial B_y)^{(n+\frac{1}{2})}_{i+\frac{1}{2},j,k} \tag{2.22}$$

A partial derivative in FDTD method is discretized as:

$$(\partial_x F)_{i,j,k} = \frac{F_{i+\frac{1}{2},j,k} - F_{i-\frac{1}{2},j,k}}{\Delta x} \tag{2.23}$$

The FDTD method requires the satisfaction of the Courant–Friedrich– Lewy (CFL) condition to guarantee the stability of the method: this condition requires the time step to be smaller than:

$$\Delta t_{CFL} = [\sum_{\mu} \Delta \mu^{-2}]^{-\frac{1}{2}}, \tag{2.24}$$

where $\mu = (x, y, z)$ are the three spatial dimensions.

With the computation of the fields at the new timestep, the loop can start again.

2.3 Features of SMILEI

So far, the structure of a PIC codes in general has been described. In this section, specific characteristics of SMILEI are discussed.

SMILEI doesn't employ the international system of units to express quantities. Instead, a normalized system of units is adopted. Velocity, electric charge and mass are normalized with respect to the speed of light (c), the absolute value of the electron charge (e) and the electron mass (m_e), respectively. As for the time, it is normalized with respect to ω_r^{-1}, with ω_r being a reference angular frequency; for a simulation involving the irradiation of plasma with a laser, the reference angular frequency is set equal to the laser one. Space is normalized with respect to c/ω_r. Normalization factors for other quantities are reported in 2.2 [19].

Units of velocity	c
Units of charge	e
Units of mass	m_e
Units of momentum	$m_e\, c$
Units of energy, temperature	$m_e c^2$
Units of time	ω_r^{-1}
Units of length	c/ω_r
Units of number density	$n_r = \epsilon_0\, m_e\, \omega_r^2/e^2$
Units of current density	$e\, c\, n_r$
Units of pressure	$m_e\, c^2\, n_r$
Units of electric field	$m_e\, c\, \omega_r/e$
Units of magnetic field	$m_e\, \omega_r/e$
Units of Poynting flux	$m_e\, c^3\, n_r/2$

Figure 2.2: Normalization factors used in SMILEI

PIC codes are so computationally expensive that normal calculators would not be able to complete a simulation in a reasonable amount of time and that is why SMILEI is designed to work through high-performance computing (HPC). The main idea of HPC is the use of more CPUs (also called cores) to work on the same memory. More precisely, the cores of a supercomputer are grouped in nodes, and all cores belonging to a node share the same memory. Software-wise, the instructions are grouped in threads, which are distributed among the nodes, and threads computed by the same node are called a process. This structure is graphically shown in 2.3.

The computational domain is split into small portions called patches, which are then assigned to the various cores. The main advantage of this management of the computational resources, based on a grid-based decomposition rather than a particle-based one, is to avoid the need of communication between cores to compute the magnetic field at a certain location. On the other hand, a load imbalance might arise: if number density varies considerably between patches, cores will be burdened by different computational load, which might lead to an inefficient use of computational resources. On SMILEI it is possible to activate a feature called load balancing, which, at intervals, redistributes patches among cores with the aim of making the wordload distribution as uniform as possible.

SMILEI's basic algorithm does not reproduce all physical phenomena characterizing a plasma. For this reason, some physical modules are implemented and can be included in the set-up of a simulation to account for desired processes, if needed. In the remaining part of this section, some of these modules are briefly discussed.

Vlasov equation, 2.2, was written for a collisionless plasma. The theory of

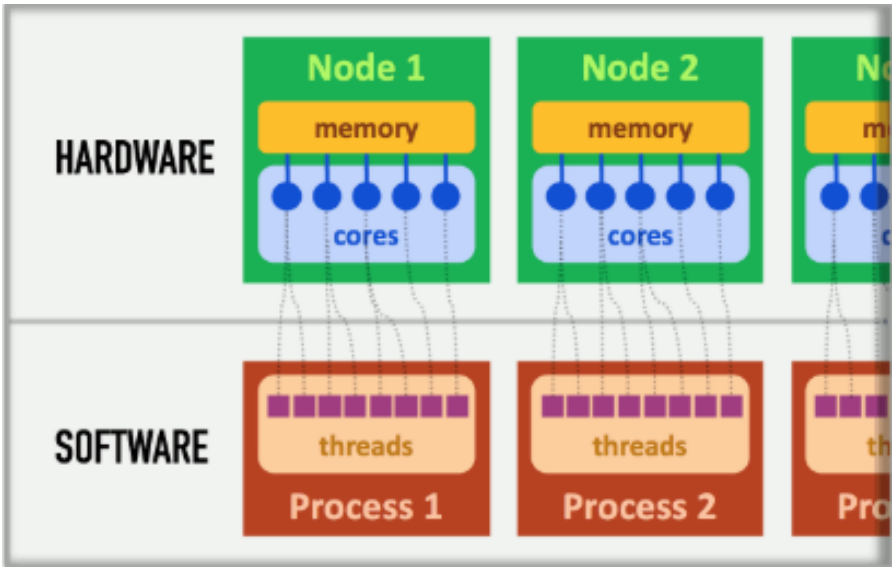

Figure 2.3: A schematic representation of the subdivision of supercomputers in nodes, cores, threads and processes. Image from SMILEI website's guide.

collisions implemented is described in [20], which assumes, for a given particle, several collisions during a timestep. In the Coulomb collision, distant collisions with a small scattering angle are much more dominant than close collisions and therefore a deflection angle $\theta << 1$ is assumed for each of these collisions. Both intra-particle collisions (between particles of the same species) and inter-particle collisions (between particles of different species) can take place. Quasi-particles are randomly paired, so that, during each time-step, a macro-particle collides with only one other. Pairs are picked among particles contained in the same patch. A difference in the implementation of this module, with respect to [20], is the use of a modified distribution for the deflection angle. Given Nanbu's $s$parameter and a random number U in the interval [0,1], the deflection angle χ is:

$$\sin(\frac{\chi^2}{2}) = \begin{cases} \alpha U/\sqrt{1-U+\alpha^2 U}, & \text{if } s < 4 \\ 1-U, & \text{otherwise} \end{cases} \tag{2.25}$$

where $\alpha = 0.37s - 0.005s^2 - 0.0064s^3$.

Another fundamental phenomenon involved in laser-plasma simulations is ionization. As far as collisional ionization is concerned, this is implemented in the ionization module, while for field and barrier suppression ionization a different module exists.

Other modules allow the implementation of more advanced processes that normally do not take place or can be neglected, but that become relevant when

specific conditions are met, e.g. when laser intensity is larger than a certain threshold . In such cases, neglecting them can result in an inaccurate simulation of the real behaviour of a plasma. Such modules include: multi-photon Breit-Wheeler pair production, high-energy photon emission and radiation reaction. For more information on the mathematical implementation of these physical processes, SMILEI's website documentation provides a detailed and extensive explanation.

One last point needs to be remarked: several quantities introduced by the modules cannot be normalized to dimension-less terms. Therefore, when including them in a simulation, a value for the reference angular frequency expressed in international system units needs to be provided in the input file.

Chapter 3

Kinetic modeling of laser absorption in foams

In this chapter PIC code Smilei is used to simulate the interaction of a laser beam irradiating the structural element of a subcritical foam. First, physical and computational parameters will be detailed. Then, results of simulations will be shown and discussed. In particular, two cases, differing in the polarization of the laser, are investigated, and differences between these two different configurations are discussed. Furthermore, a third simulation with a variation of the value of the diameter, presented in the last section, illustrates how a different dimension influences the evolutiono of the target.

3.1 Simulation parameters and physical set-up

The simulations performed in this chapter are based on the work done in [16]. The paper first provides a theoretical description of the interaction of a laser with a single foam element, applying Mie theory to the case of a target of cylindrical shape; this theoretical model was already presented in chapter 1. In the second part of the paper, the behaviour predicted by theory is then compared to the results of two simulations.

As said, the simulations focus on a single fibre element of the foam: this fibre is modelled as a cylinder, which is surrounded by a void region. The geometry of the simulation is depicted in 3.1.

The cylinder axes is directed along the z-direction, and its base lies in the x-y plane. The radius of the cylinder is a_0, the cell has a square base whose side is l_p The pore and the cylinder have the same height, which is l_c, .

The x-axes is taken as the direction of propagation of the laser. For simplicity, a linearly-polarized beam is considered, and two cases are then considered: one

where the electric field is directed along the y-direction, and a second where it's directed parallel to the z-axes. The paper, as a convention for the definition of the polarization state, considers the x-z plane as the plane of incidence. Therefore, **E** directed along z is considered as P-polarization, while the S-polarization has **E** along y.

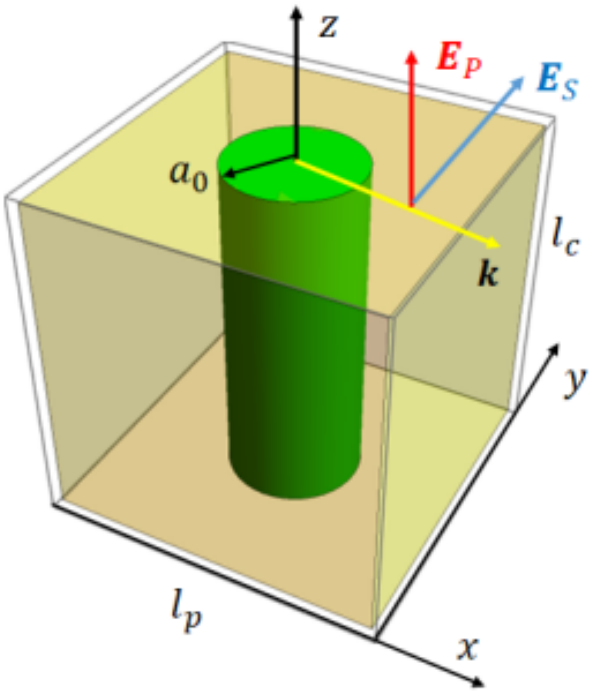

Figure 3.1: Representation of the foam fiber and void cell. Directions of the electric field of the linearly-polarized laser are indicated for P- and S- polarizations by E_P and E_S, respectively

The domain of the simulation is a plane parallel to the x-y plane, irradiated by a plane-wave beam propagating along x-direction from left to right. The laser, which is linearly polarized, has an intensity I_0 of $10^{14} W/cm^2$ and a wavelength $\lambda = 0.35 \mu m$.

The computational domain has the same length along both direction, which is $L_x = L_y = l_p = 2.239 \mu m$. The cylinder, placed at the center of the domain, has a radius $a_0 = 0.1 \mu m$. The filament is assumed to be already completely ionized; its effective charge $Z_{av} = 4.54$, the mass of the ions is $8.73 m_p$, where m_p is the mass of the proton. Both ions and electrons are initialized with the same temperature $T_e = T_i = T = 1eV$ and a zero average velocity.

The cylinder has a uniform number density. As for the electrons, their density

is initialized to $35n_{cr}$, where n_{cr} is the plasma critical density. The plasma is electrically neutral, and therefore the ion density is scaled by a factor $1/Z_{av}$ with respect to the electron density.

The domain is discretized into 1536 cells along each direction, corresponding to a cell length $\Delta x = \Delta y = 0.0262$, in normalized units. Taking into account the parameters of this simulation, the Debye length in normalized units is (in SMILEI's normalized units, the electric charge and the void dielectric constant have a unitary module):

$$\lambda_D = \sqrt{\frac{T}{n_e}} \approx 2.36 \times 10^{-4} \tag{3.1}$$

The cell length adopted is around 111 times the Debye length; with this level of resolution, numerical heating can be expected to a certain degree. However, the Debye length is inversely proportional to the electron density, and since the cylinder expands in the pore, the number density greatly decreases. As a consequence, after some ps the Debye length increases and the chosen resolution is in the order of the Debye length.

As for the time discretization, the timestep was set to 0.99 the limit value stated in 2.24, so that stability is guaranteed. The simulation time was set to 8 ps and 10 ps for P-polarization and S-polarization, respectively.

The simulation is initialized with particles only in the region of the cylinder. Since the particles, eventually, will be spread all over the domain, an adequate number of particles per cell is required to be set in order to have statistically relevant results. The aim is to have around 9/10 particles per cell, assuming them to be spread in all cells. It is then possible to write:

$$nppc_I = nppc_f \frac{A_{tot}}{A_{cyl}}, \tag{3.2}$$

where A_{tot} and A_{cyl} are the total and the cylinder areas, while $nppc_I$ and $nppc_f$ are the initial and final values of number of particles per cell. A value of 1500 particles per cell was chosen.

Collisions between particles are considered. Since the collision module is used, a reference angular frequency in SI units needs to be specified, and it was set to the value of the laser one. Knowing the laser wavelength, it is easily calculated as:

$$\omega_r = \frac{2\pi c}{\lambda} \approx 5.38 \times 10^{15} s^{-1} \tag{3.3}$$

3.2 S-polarization

In this section the results of the simulation with S-polarized laser are presented. The plots showing charge density and energy distributions are along the x axes, cutting through the centre of the cylinder (in international system units, $y = 1.1\mu m$).

Charge density distribution plots are expressed in units of critical density. Since electrons have a unitary charge in normalized units, electron charge density $q_e = n_e \times |e|$ is just equal to their number density n_e. As for the ions, their charge is Z_{av} times the electron charge; therefore, ions charge density is $Z_{av} \times n_i$. Net charge is calculated as $q_{net} = q_i - q_e = Z_{av} \times n_i - n_e$. Vertical dotted lines indicate initial the position of the target.

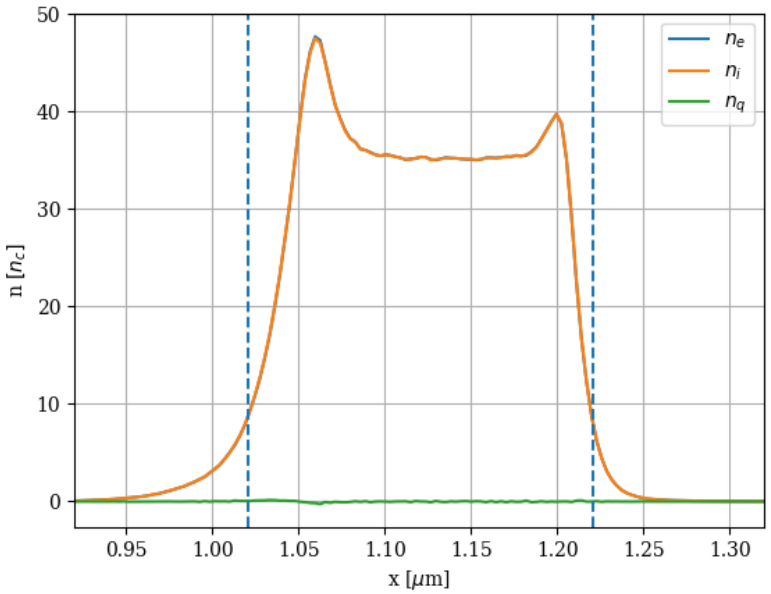

Figure 3.2: Charge density distributions of ions, electrons and net charge along x at y = $1.1\mu m$, at 0.5 ps - S polarization case.

Figures 3.2 and 3.3 show the charge distributions at 0.5 and 1.0 ps. In the first part of the interaction the cylinder undergoes a compression due to the formation of a pressure wave which, as it can be observed by comparing the distributions at two time instants, travels inward. The dynamic of the cylinder density and the formation of the wave are linked to the mechanisms of absorption.

Initially, the target is a homogenous, over-dense plasma surrounded by vacuum. Plasma has a pressure which is proportional to its number density and temperature, $p_e = nT$; given the large step density gradient, the natural behaviour of plasma

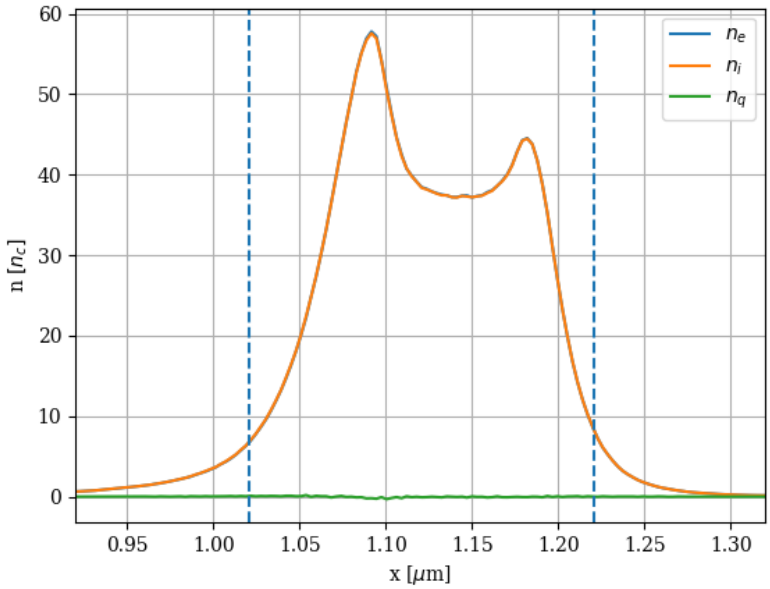

Figure 3.3: Charge density distributions of ions, electrons and net charge along x at y = $1.1\mu m$, at 1.0 ps - S polarization case.

would be to expand in the void space enclosing it. The resulting outward pressure is opposed by a compression driven by the laser, explaining why the compression takes place.

Since the electron density is much higher than the critical value, the laser is not able to penetrate through the whole target, and the interaction is instead localized close to the surface. Here absorption takes place by electrons, normally taking place by inverse Bremsstrahlung; however, in the case under analysis, when the laser has a component of the electric field normal to the density gradient and the target is over-dense, another mechanism can take place. In a first half-cycle the electrons are pulled out of the plasma, and in the second one they're accelerated inward, where they deliver the energy acquired; this mechanism is called vacuum heating, first proposed by Brunel [21] [22], and it's more efficient than inverse Bremsstrahlung.

Brunel heating arises when the density gradient is steep, which is the condition at the boundary of the cylinder during the first pico-seconds. As the cylinder starts expanding, after the compression phase, the gradient of n_e becomes smoother, and resonant absorption can become dominant. This phenomenon, like vacuum heating, is possible only in presence of a component of the electric field is parallel to the density gradient. Resonant absorption takes place when the plasma frequency is equal or close to the frequency of the incoming wave e, and it's more efficient when

the density gradient is smoother [21]. As a result, during the expansion phase energy absorption is enhanced by the inhomogeneity of the cylinder.

As a result of the absorption, electrons heat up and their kinetic energy increases. The plasma becomes hotter and electrons are ablated from the surface. By leaving the cylinder, a charge imbalance and a consequent electric field close to the surface are formed; the latter is the driver for the acceleration of ions in the absorption region, which do not interact directly with the laser. This mechanism is analogous to a technique employed for the acceleration of ions called target normal sheath acceleration [23].

The ablation of particles drives a reaction on the target, similar to the rocket effect, which is the origin of the compression wave observed in the plots. It is worth noting that laser impact can drive a pressure by another mechanism, driven by the ponderomotive force, which drives particles from outside regions of high electric field. For a laser intensity lower than $10^{16} W/cm^2$ the ablative pressure is dominant, and therefore radiation pressure, the one driven by ponderomotive force, can be neglected [24].

The plots actually show the formation of two peaks: a larger one on the side of incidence of the laser wave and a smaller one on the opposite side, both travelling toward the centre. For an S-polarized laser the distribution of absorption is extended to the flanks of the cylinder due the normal component of the electric field, with higher absorption rates on the incidence side, as depicted in figure 3 of [16]. Since the energy is absorbed on both sides, two compression waves are formed, with the higher peak reached on the side of larger laser absorption.

The compression phase can be observed also in figures 3.4 and 3.5, which depict the distribution of the number density of ions at 0.5 and 1.0 ps. The cylinder is compressed, the front of peak density shrinks towards the centre and the maximum density increases.

Compression goes on as depicted in figures 3.6 and 3.7. The maximum density is reached at around 1.7 ps, with a peak of almost 70 times the critical density; at 2.0 ps the peak has lowered, highlighting that the cylinder starts expanding. As the cylinder compresses, the outward pressure driven by the pressure gradient overcomes the compression and the expansion begins. Ions and electrons progressively fill the pore and the density homogenizes reaching everywhere a density lower than the critical one, as in figure 3.8, allowing for transparency to incoming electromagnetic wave.

During the ablation process, quasi-neutrality is maintained everywhere ($n_q \approx 0$), and even during the expansion of the cylinder, where ion and electron charge distributions do not overlap anymore, the net charge density is still relatively small.

Ablation and expansion processes can be highlighted also by the energy distributions of ions and electrons. Figure 3.9 shows them during the first part of the simulation. Peak values are around 15 and 0.8 keV for ions and electrons,

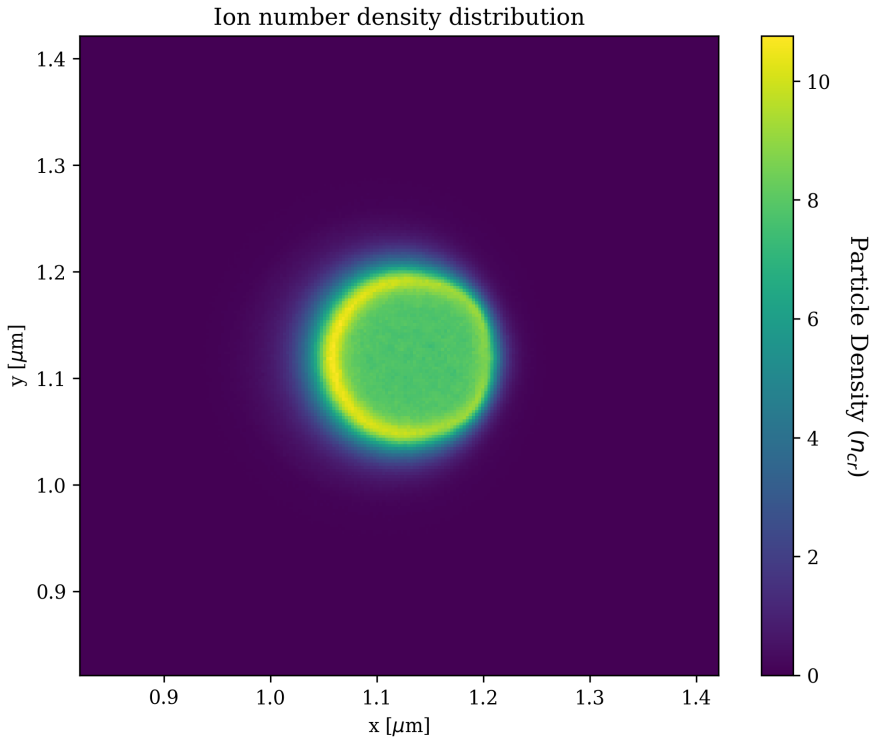

Figure 3.4: 2D distribution of ion number density at 0.5 ps - S-polarization case.

respectively. These peaks progressively move to the edges of the domain and the distributions show a partial symmetry, confirming absorption on both sides.

Once the plasma fills the cell, the energy homogenizes over time, as shown in figure 3.10; the electron energy becomes uniform on a shorter time scale, due to their lighter mass and higher intra-particle collisionality compared to ions.

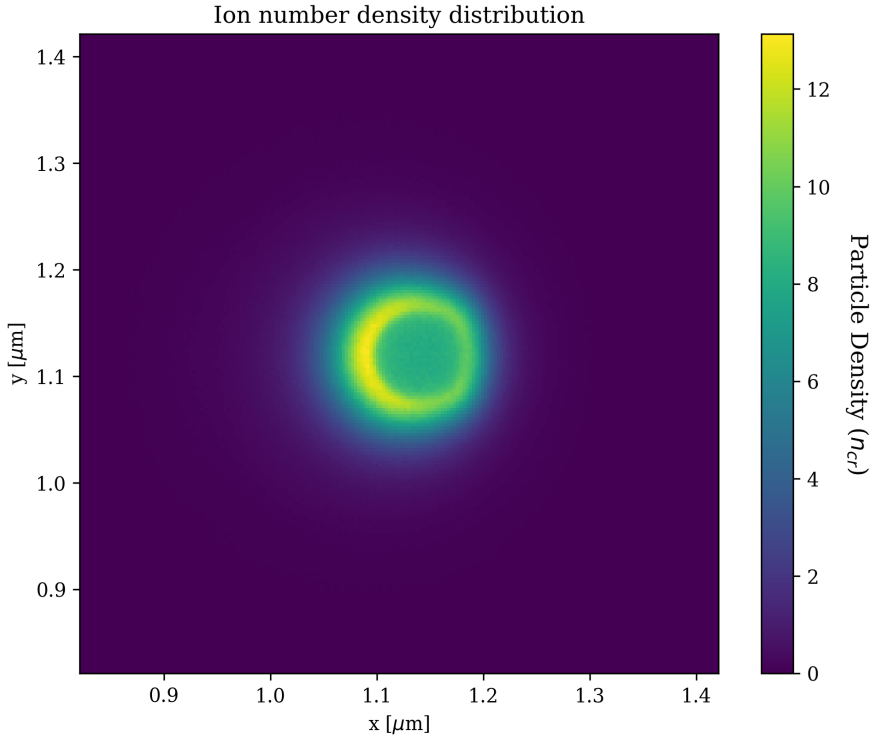

Figure 3.5: 2D distribution of ion number density at 1.0 ps - S-polarization case.

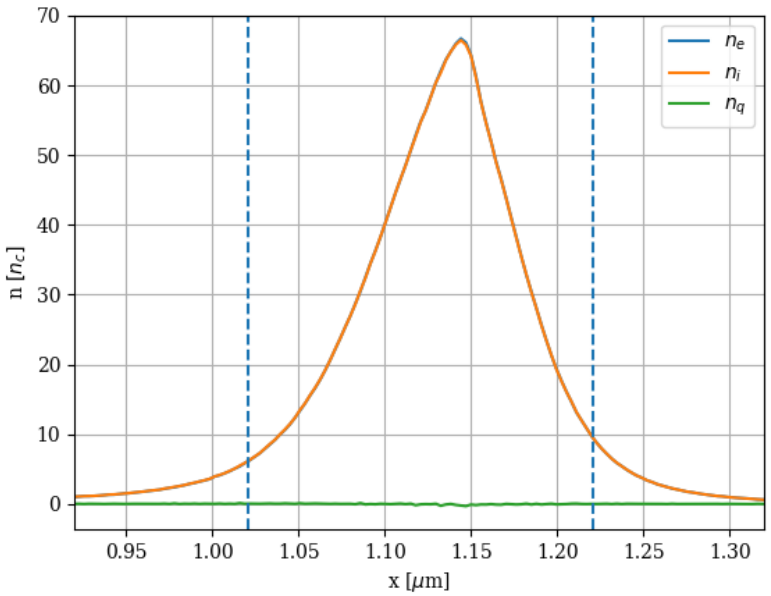

Figure 3.6: Charge density distributions of ions, electrons and net charge along x at y = 1.1μm, at 1.7 ps - S polarization case.

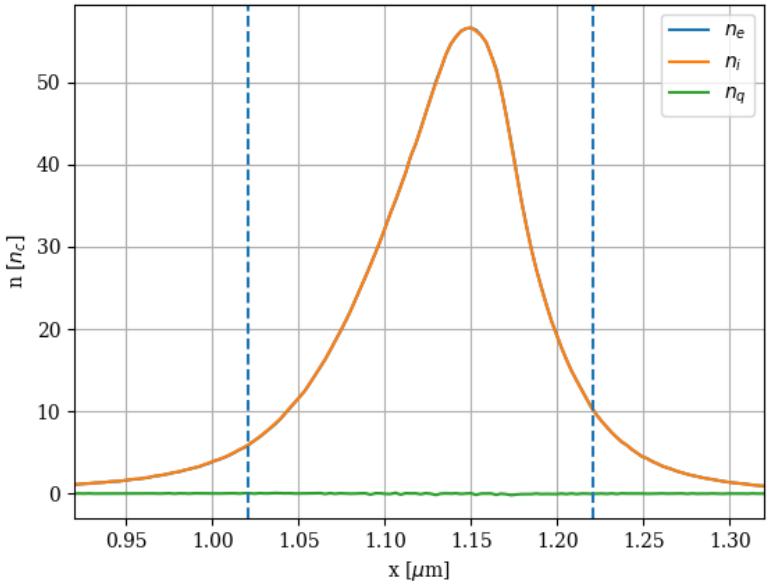

Figure 3.7: Charge density distributions of ions, electrons and net charge along x at y = 1.1μm, at 2.0 ps - S polarization case.

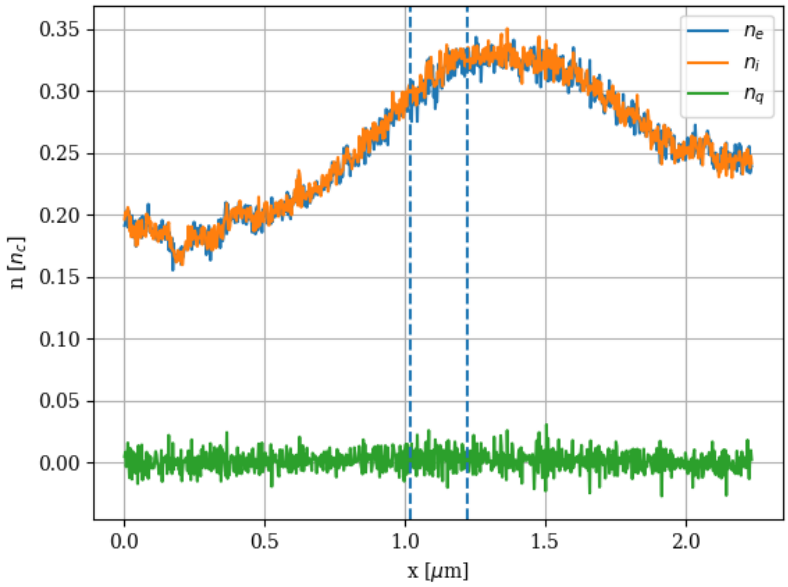

Figure 3.8: Charge density distributions of ions, electrons and net charge along x at y = $1.1\mu m$, at 8.0 ps - S polarization case.

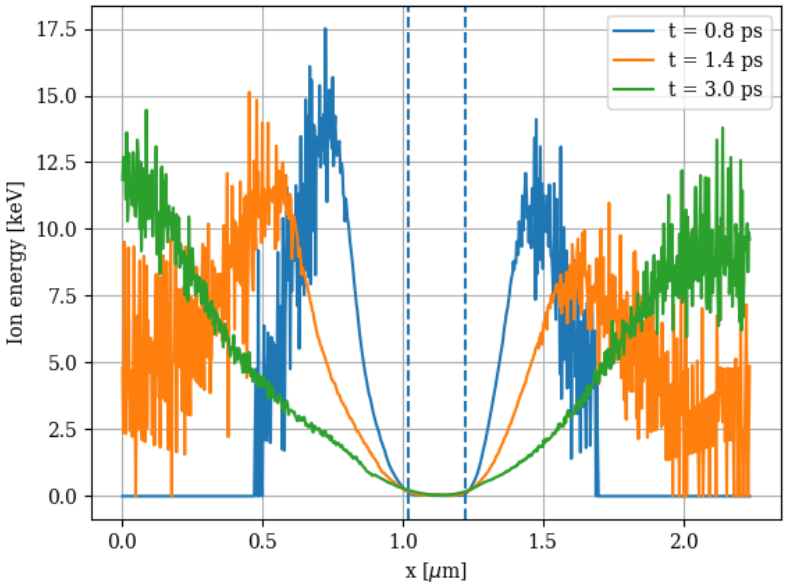

(a)

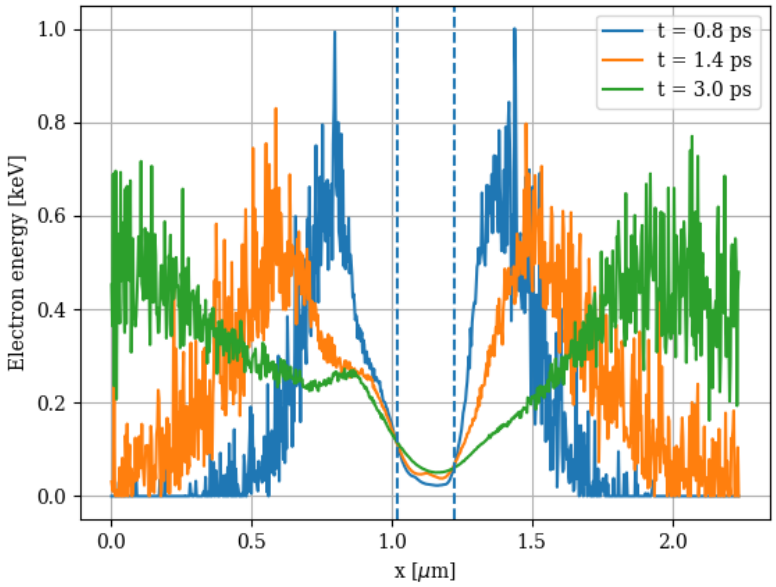

(b)

Figure 3.9: Energy distribution along x at y = 1.1μm of (a) ions and (b) electrons at 0.8, 1.4 and 3.0 ps - S-polarization case.

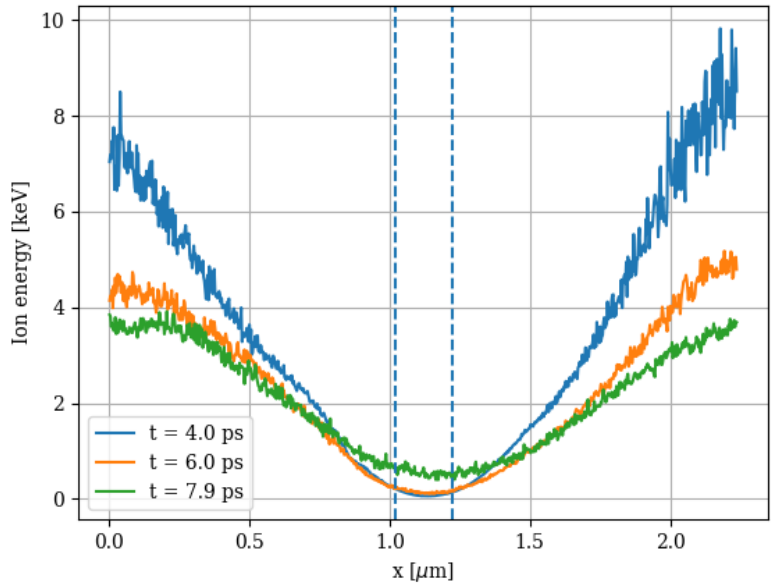

(a)

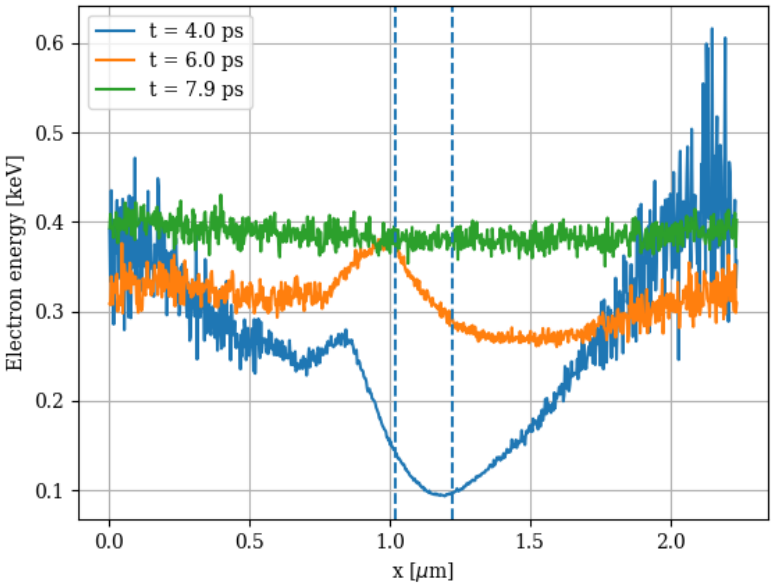

(b)

Figure 3.10: Energy distribution along x at y = 1.1μm of (a) ions and (b) electrons at 4, 6 and 7.9 ps - S-polarization case.

The energy absorbed by particles can be computed as the difference between the total kinetic energy at a given time t and the initial total kinetic energy. This distribution is presented in the plot 3.11. The quantity depicted gives an information on the absolute energy absorbed; in order to quantify the efficiency of absorption, this quantity needs to be compared to energy carried by the laser. The absorption efficiency is then defined as

$$\epsilon_{abs}(t) = \frac{E_K(t) - E_K(0)}{E_{Poy}(t)}, \tag{3.4}$$

where $E_{Poy}(t)$ is the time-accumulated Poynting contribution through left boundary. The absorption efficiency, in figure 3.12 after around 2 ps starts increasing steadily up to 6 ps. This boost of the absorption efficiency is driven by the process of resonance absorption described above; 2 ps is indeed when the expansion begins and the particle density gradient becomes less steep.

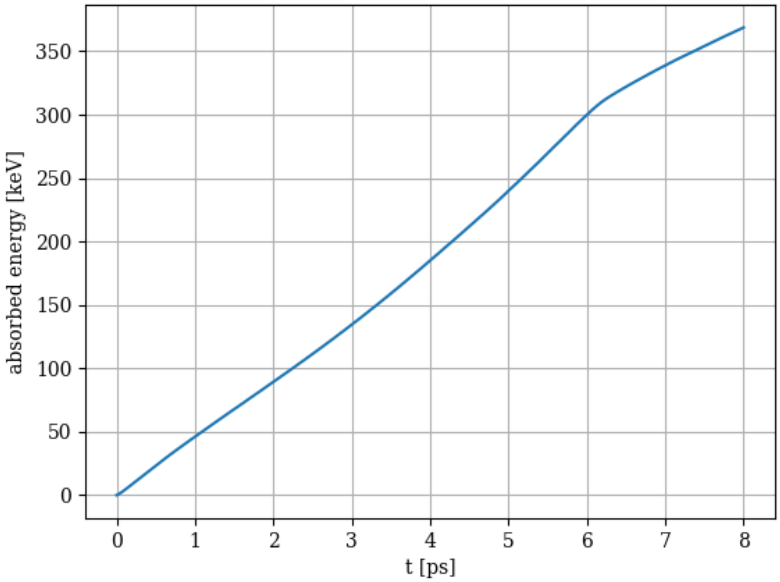

Figure 3.11: Evolution in time of energy absorbed by particles - S-polarization case.

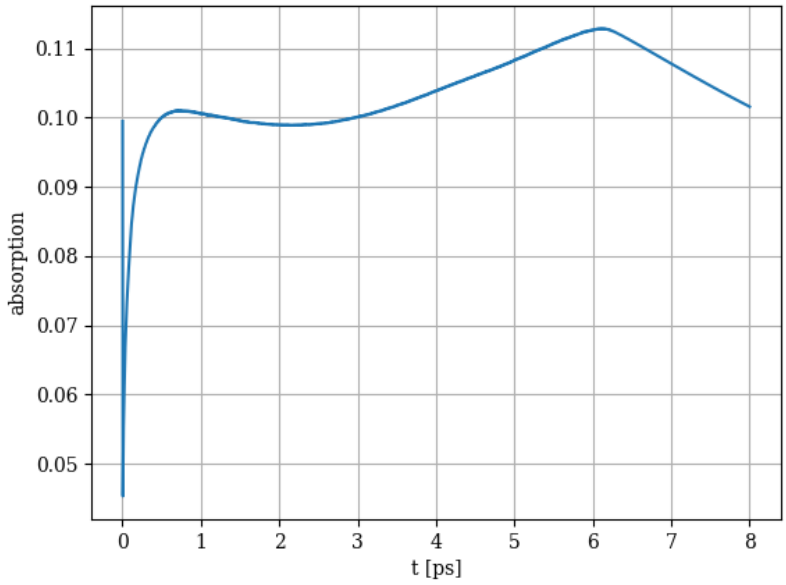

Figure 3.12: Evolution in time of energy absorption efficiency by particles - S-polarization case.

3.3 P-polarization

In this section results from the simulation with P-polarized laser are presented. The cylinder evolution still follows the processes of absorption, ablation, compression and expansion, though exhibiting some differences which boil down to the different absorption mechanism and extension.

A compression wave is formed again, as depicted in figure 3.13, with the charge density distribution at 1 ps. Differently from S-polarization, the compression takes place only on the side of cylinder irradiated by the beam: due to the absence of the normal component of the electric field, the angular distribution of the electric field is less extended and limited to the surface facing the beam.

Compared to S-polarization, here much higher densities are reached, and density evolution takes place during longer time scales; in particular, the peak value of electron density in normalized units is around 110, reached after 2.7 ps (for S-polarization it was around 65, after 1.7 ps). The processes enhancing absorption described in the previous section do not take place here; when electrons oscillating due to the electric field collide with ions, the energy absorption and its transfer to ions takes place. Therefore, the mechanism is collisional, which is less effective than resonance. The particles carried by the compression wave are less energetic and collisional heat transfer is slower. As a consequence the outward plasma pressure opposing to the compression is weaker than the one of S-polarization case, explaining why, for the case under consideration, the compression takes place for a longer time and the density is much higher.

The asymmetry in energy absorption between the two sides can be highlighted also by the distributions of ion and electron energy in figures 3.15: higher values are reached on the left side, and the gap is much larger for electrons, which are the ones directly interacting with the laser. The plots refer to the same time instants as 3.9: peak values for P-polarization case are around one third of the S-polarization ones, confirming a less efficient energy absorption.

The increase of total kinetic energy by the particles is illustrated in 3.16. The energy absorbed is much lower compared to the one of the previous section: at 8 ps the increase has a value of about 160 keV, while it was 360 keV for an S-polarized laser.

As for the efficiency of the absorption, observable in 3.17, after around 2 ps it increases steadily driven by collisions, without exhibiting the peak attributed to resonance as in S-polarization case, peaking at the end to 0.05.

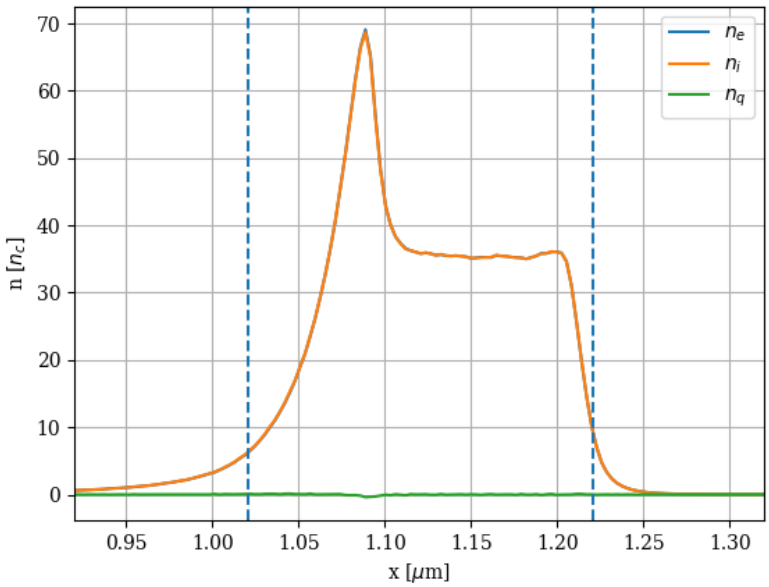

Figure 3.13: Charge density distribution along x at y = 1.1μm of ions, electrons and net charge at 1.0 ps - P-polarization case.

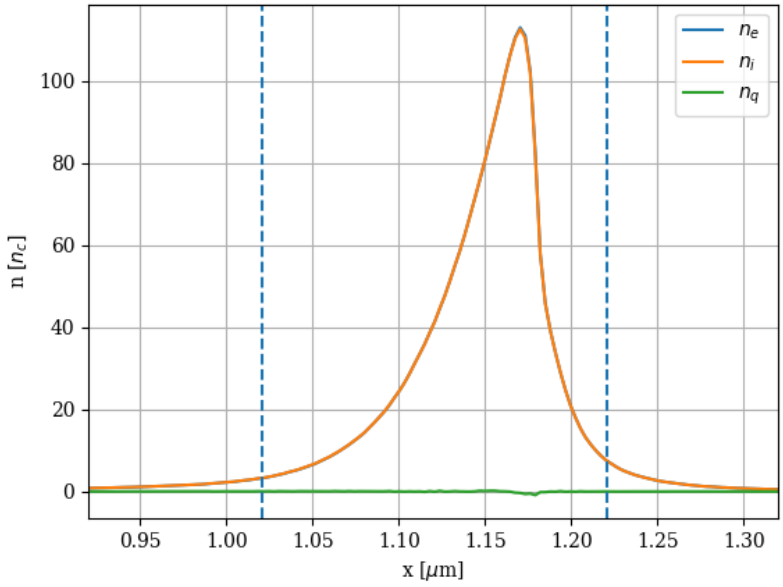

Figure 3.14: Charge density distribution along x at y = 1.1μm of ions, electrons and net charge at 2.7 ps - P-polarization case.

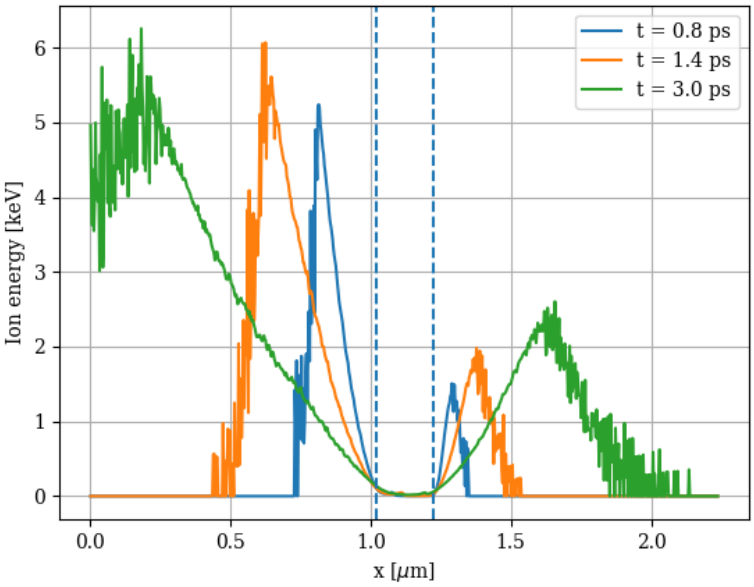

(a)

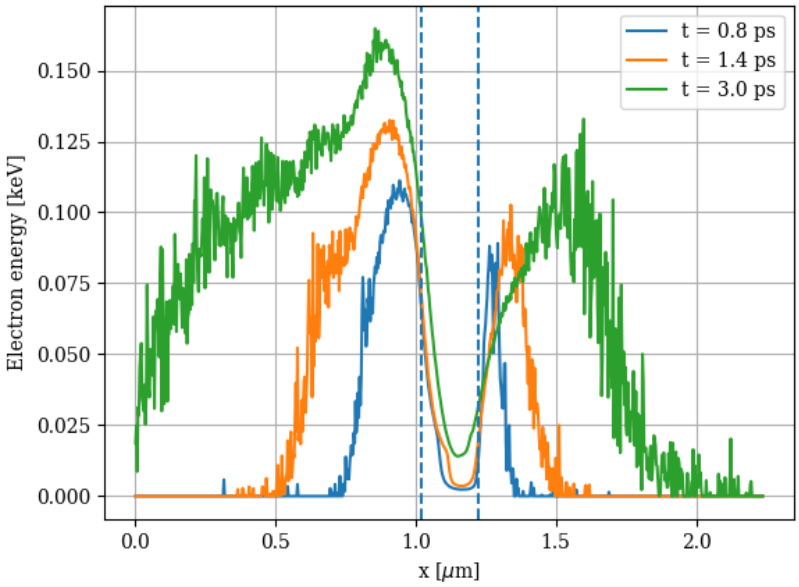

(b)

Figure 3.15: Energy distribution along x at y = 1.1μm of (a) ions and (b) electrons at 0.8, 1.4 and 3.0 ps -, P-polarization case.

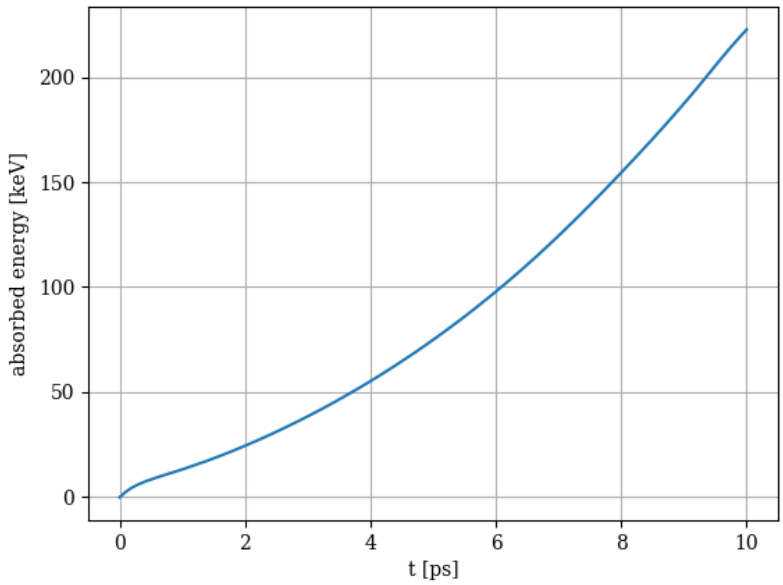

Figure 3.16: Evolution in time of energy absorption efficiency by particles - P-polarization case.

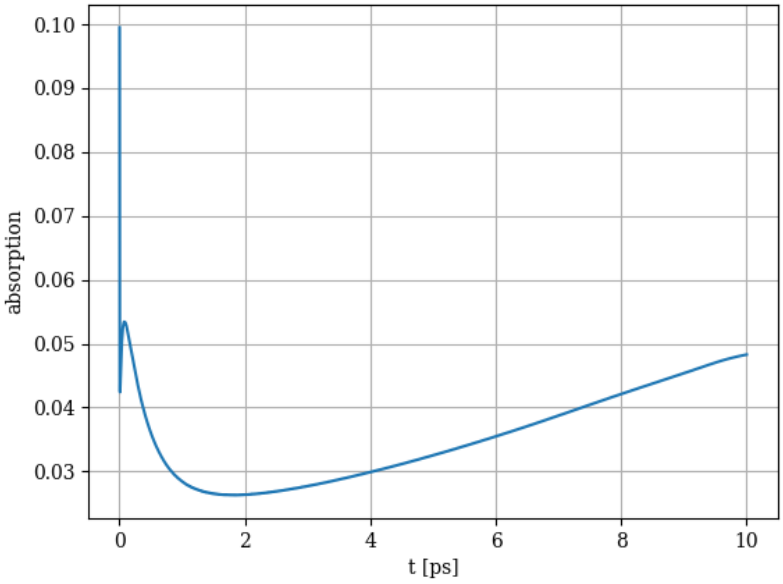

Figure 3.17: Evolution in time of energy absorption efficiency by particles - P-polarization case.

3.4 Diameter larger than the wavelength

The simulations of the previous two sections involved a target whose diameter was smaller than the laser wavelength. In this section the results from a new simulation where the diameter value is larger than the wavelength are presented. The radius new value is $a_0 = 0.2\mu m$, and therefore $D = 0.4\mu m > \lambda = 0.35\mu m$. The case under consideration is that of an S-polarized laser.

Figure 3.18 shows the charge density distributions at 2.0 ps. Because of the larger dimension of the diameter, the time-scales of evolution are longer than the sub-wavelength case: while in the latter started the expansion around 2 ps, here the cylinder is still in the phase of contraction. Peak of density is reached at around 4.0 ps, pictured in 3.19. The peak value is around 130 times the critical density, which is around two times the one in figure 3.2.

As for the distributions of energy of electrons and ions, figures 3.20 and 3.21, the highest energy values reached are around 0.25 keV and 6 keV, respectively. Compared to the sub-wavelength case, these values are around one half to one third. The plots also exhibit a higher degree of asymmetry between the two sides, suggesting that the the absorption on the flanks of the cylinder is less prominent compared to what observed for the sub-wavelength simulation.

Figures 3.22 and 3.23 show the energy absorbed and the absorption efficiency, respectively. In order to compare these results with the one of the first section, it must be noted that the present results refer to a larger number of particles. Since the initial number density was still set to $35n_{cr}$ and the cylinder has a radius the is two times the original one, the total number of particles is four times the one of the first case; at 8 ps the absorbed energy is around 700 keV, which is almost the double of the value at the same time in figure 3.11. A similar consideration needs to be done for the absorption efficiency, since the geometrical cross section of the cylinder has increased but the side of the domain is still the same, and therefore the target "sees" more of the incoming wave. To make a rough comparison, we could imagine to double the side to keep the same proportion of l_p/D. If we assumed the laser energy entering the system from the left boundary to be proportional to its length, the energy entering the system would double. As a result, the efficiency would be half of the value shown and be around 0.1 at 8 ps, as for the sub-wavelength configuration.

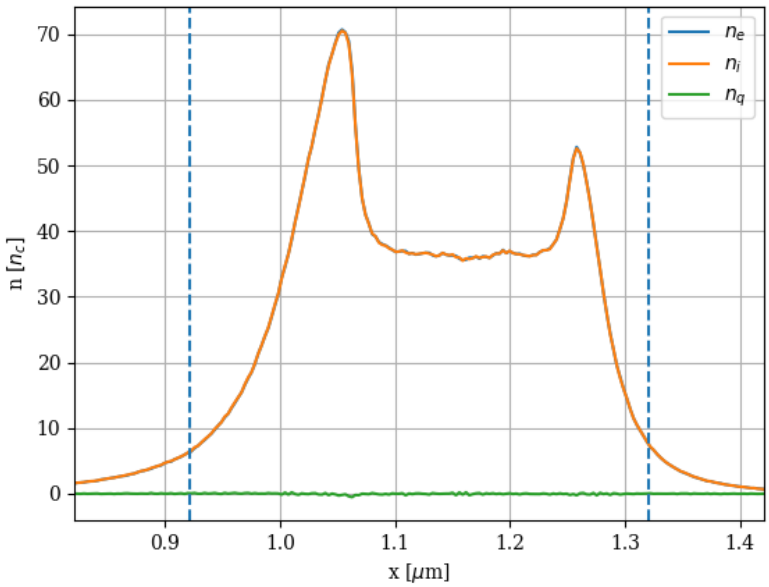

Figure 3.18: Charge density distribution along x at y = 1.1μm of ions, electrons and net charge at 2.0 ps - diameter larger than wavelength, S-polarization case.

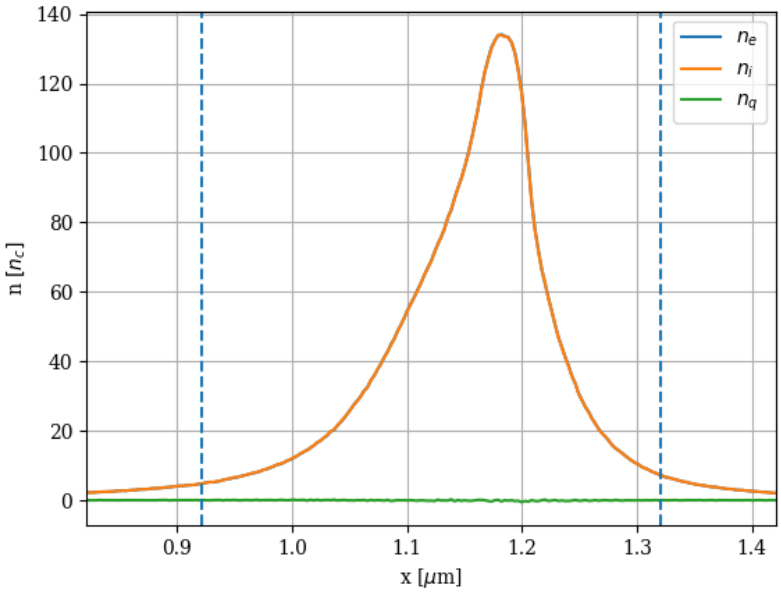

Figure 3.19: Charge density distribution along x at y = 1.1μm of ions, electrons and net charge at 4.0 ps - diameter larger than wavelength, S-polarization case.

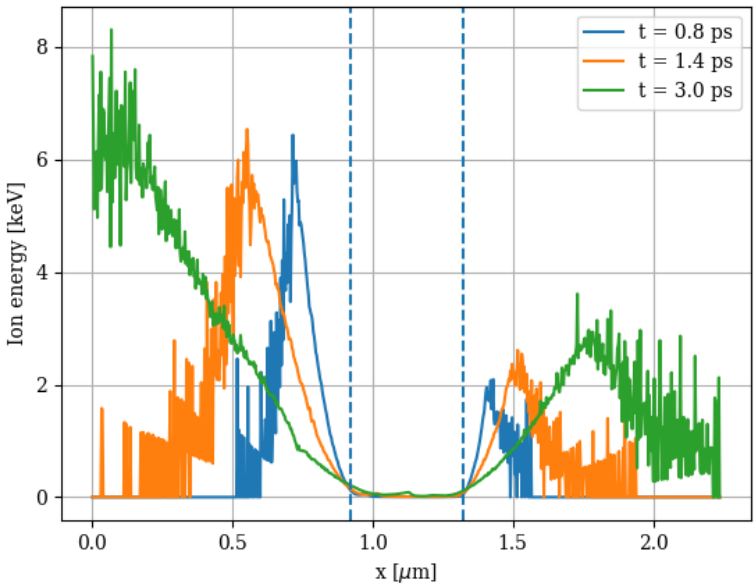

Figure 3.20: Energy distribution along x at y = 1.1μm of ions at 0.8, 1.4 and 3.0 ps - two-dimensional, diameter larger than wavelength, S-polarization case.

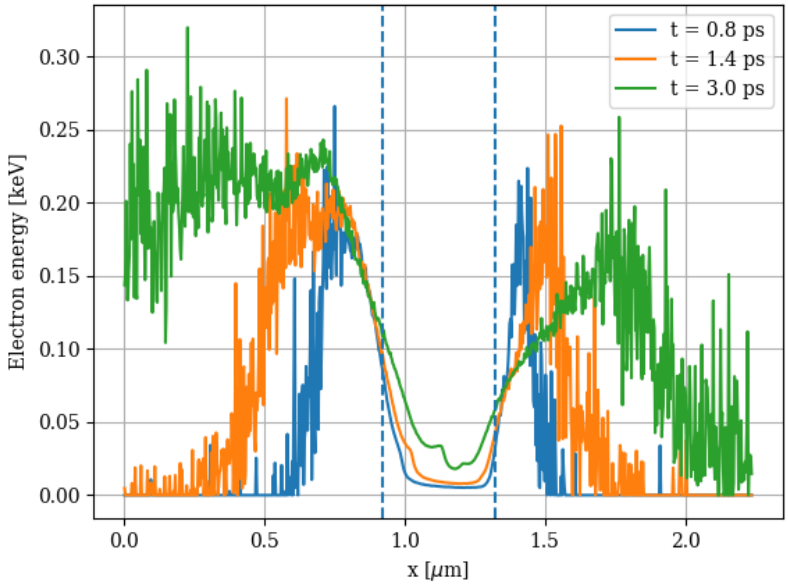

Figure 3.21: Energy distribution along x at y = 1.1μm of electrons at 0.8, 1.4 and 3.0 ps - two-dimensional, diameter larger than wavelength, S-polarization case.

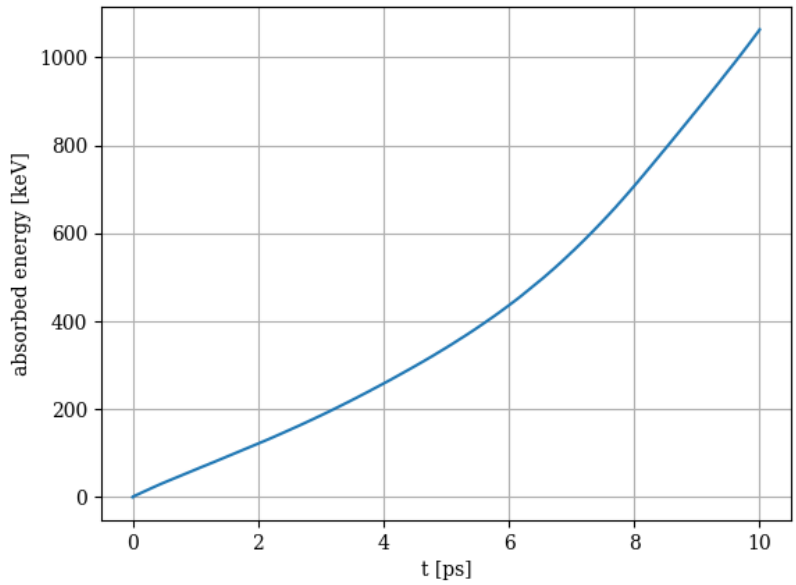

Figure 3.22: Evolution in time of energy absorption efficiency by particles - diameter larger than the wavelength, S-polarization case.

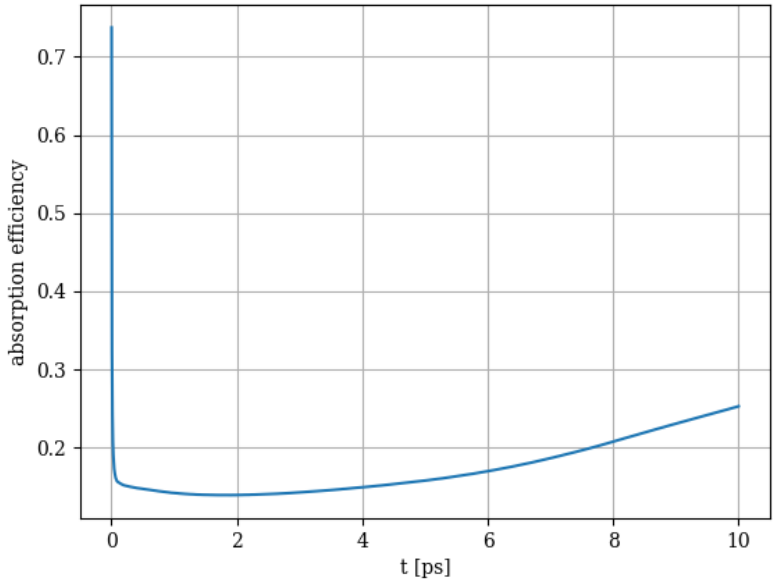

Figure 3.23: Evolution in time of energy absorption efficiency by particles - diameter larger than the wavelength, S-polarization case.

Chapter 4

Effect of multiple ion species in laser absorption by foam element

In chapter three, the interaction of a laser beam with a foam structural element was investigated assuming the presence of a single ion species. Foams are usually made of two or more elements which will behave differently due to their different mass and charge, affecting the evolution of the processes the plasma undergoes.

This chapter is devoted to analyse the effects of considering the presence of two different ion species. The physical set-up is the same as the one of simulations of chapter 3, keeping the average mass and charge the same. A comparison between then new results and the old ones allows us to understand what's the influence of considering two elements in the energy absorption mechanisms.

4.1 Introduction

The simulations presented in the previous chapter considered a foam structural element to be already completely ionized and turned into a plasma. Foams are usually made of materials that are compounds of two or more elements, usually carbon, hydrogen, oxygen and beryllium [13]. As a result, ions with different masses and charges will be present when the target is ionized, and the process of absorption of laser energy will be affected. The main factor that drives a different behaviour with respect to a homogenized plasma is the different charge-to-mass ratio of the ions, as it will be pointed out.

In the following paragraphs results of simulations with the same physical configuration of the ones discussed in chapter 3 are presented. These new simulations

will consider two different ion species, namely hydrogen (H^+, with atomic mass $A = 1$ and charge $Z = 1$) and fully-ionized carbon (C^{6+}, with atomic mass $A = 12$ and charge $Z = 6$). The initial number density of electrons is still 35 times the critical density, while the initial number densities of hydrogen and carbon ions were selected such that their average mass and charge match the values in chapter 3 ($m_{av} = 8.73m_p$ and $Z_{av} = 4.54$). The initial number densities n_H and n_C are easily calculated by imposing the following conditions:

$$n_H + 6n_C = n_e, \tag{4.1}$$

$$\frac{n_H + 6n_C}{n_H + n_C} = Z_{av}. \tag{4.2}$$

The first equation imposes the overall charge neutrality of the plasma; the second one that the average chargee of ions equals to Z_{av}. By solving this system, the values of n_H and n_C in function of the initial electron density are found: $n_H = 0.0643n_e \approx 2.25n_{cr}$ and $n_C = 0.1559n_0 \approx 5.46n_{cr}$.

Depending on the polarization of the laser, the results will differ greatly, and they are therefore discusses in two different paragraphs.

4.2 S-polarization

The evolution of the cylinder density still follows the processes of compression, expansion and homogenization discussed in chapter 3. In particular, the configuration with an S-polarized laser, analysed in this section, follows a similar behaviour to the homogenized case. Figures 4.1 and 4.2 show the charge density distributions of carbon, hydrogen and electrons and net charge at 1 and 2 ps. By comparing these pictures with 3.3 and 3.7, which are referred to the same time instants, one can observe that the shape of the distributions and the time scales are the same, though the peak electron density is slightly lower. The overall absorption is significantly influenced by the presence of hydrogen ions. Due to their higher charge-to-mass ratio ($Z/A \approx 1$ for protons, compared to $Z/A \approx 0.5$ for fully ionized carbon), hydrogen ions experience a greater acceleration from the sheath electrostatic field, which ultimately enhances the total energy absorption.

The energy distribution of the species are displayed in pictures 4.3, 4.4 and 4.5. Compared to the previous case, the electrons reach significantly lower peak values during the first pico-seconds; this discrepancy can be attributed to a transfer of energy to the ions (in particular, the protons) from the early stage of the interaction, while for the heavier ions of the averaged case this transfer is slower. From the ions distributions one can observe how for the hydrogen ions the filling of the pore takes place at a earlier stage and homogenization of the energy is much faster.

The different acceleration of the two ions species is also highlighted by the 2D density distribution of their densities at 1.0 ps in pictures 4.6 and 4.7 and at 4.0 ps in pictures 4.8 and 4.9. At the later time instant the front of hydrogen ions has expanded to a larger extent compared to carbon ones.

Looking at pictures 4.10 and 4.11 at 8 ps the absorbed energy is above 400 keV while the absorption efficiency is around 0.12, against 370 keV and 0.10 of the averaged case. From the plots one can conclude that in the averaged case the absorbed energy is underestimaed by around 12%.

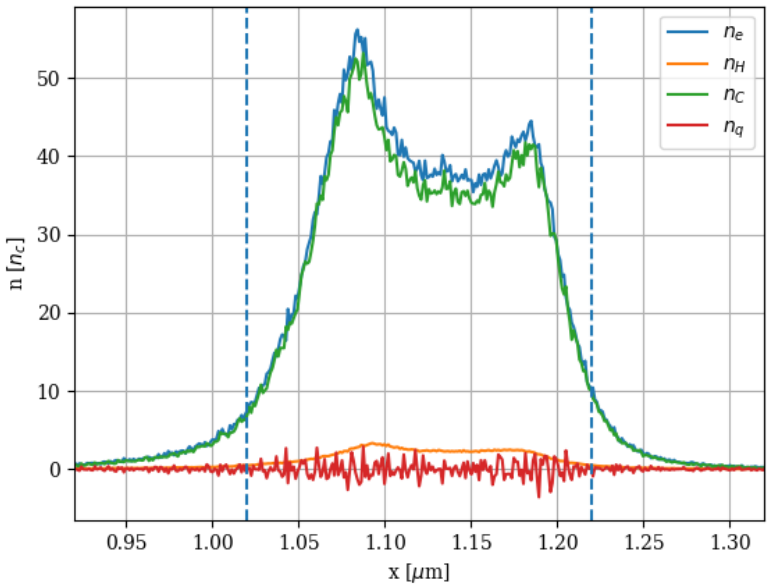

Figure 4.1: Charge density distributions of carbon, hydrogen, electrons and net charge along x at y = $1.1\mu m$, at 1.0 ps - S polarization case.

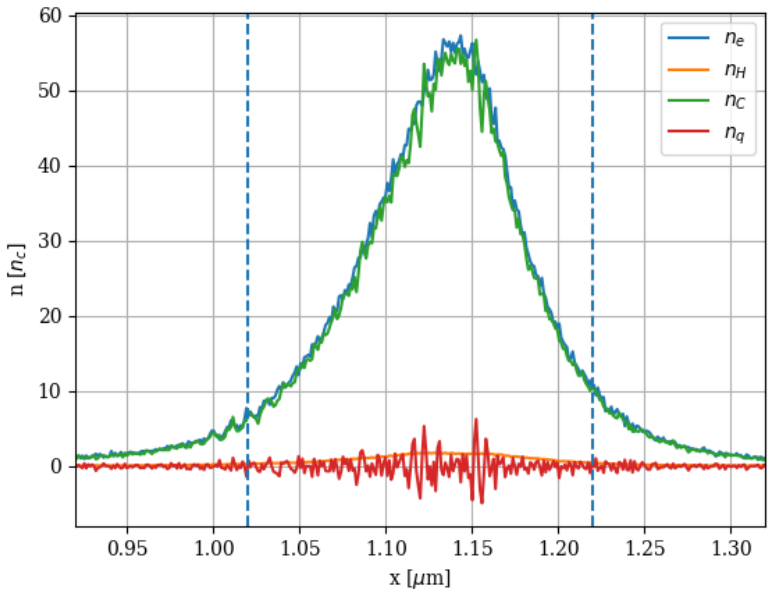

Figure 4.2: Charge density distributions of carbon, hydrogen, electrons and net charge along x at y = 1.1μm, at 2.0 ps - multispecies, S polarization case.

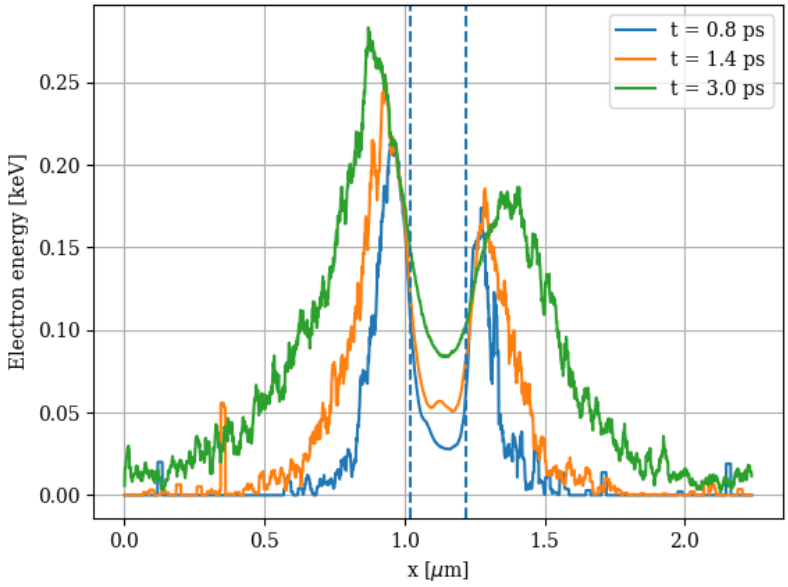

Figure 4.3: Electron energy distribution along x at y = 1.1μm at 0.8, 1.4 and 3.0 ps - multispecies, S-polarization case.

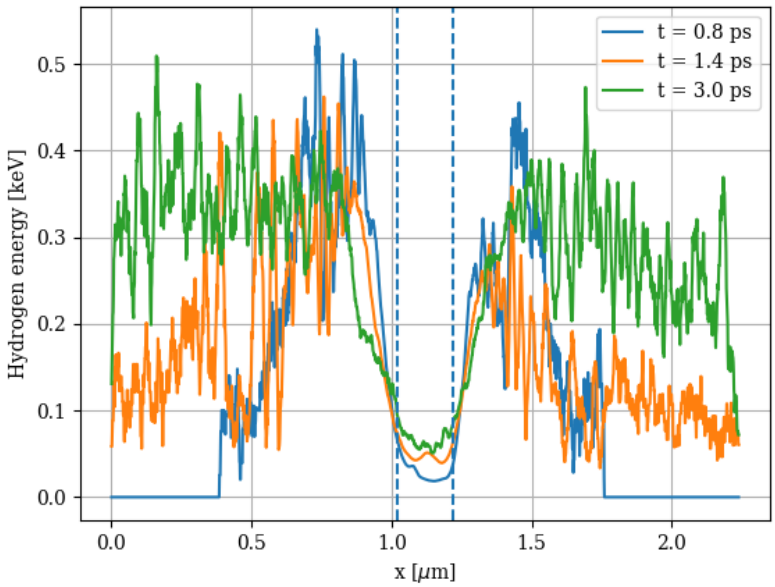

Figure 4.4: Hydrogen energy distribution along x at y = 1.1μm at 0.8, 1.4 and 3.0 ps - multispecies, S-polarization case.

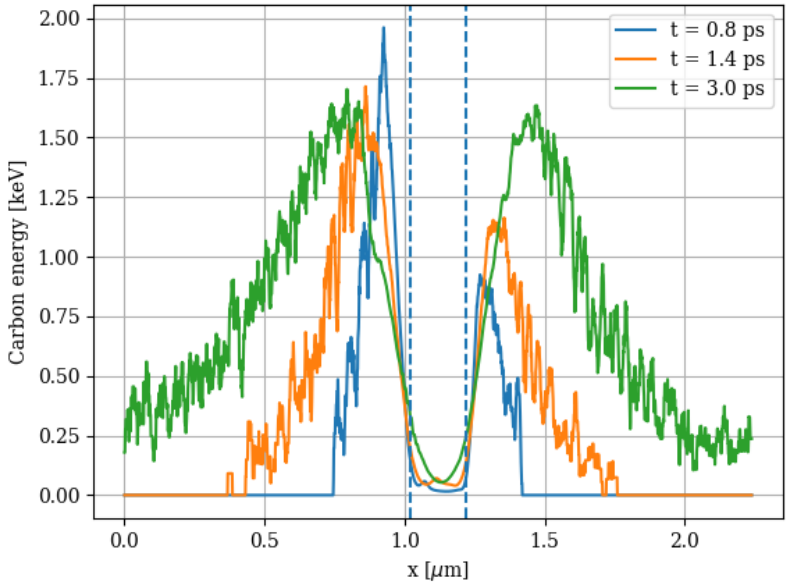

Figure 4.5: Carbon energy distribution along x at y = 1.1μm at 0.8, 1.4 and 3.0 ps - multispecies, S-polarization case.

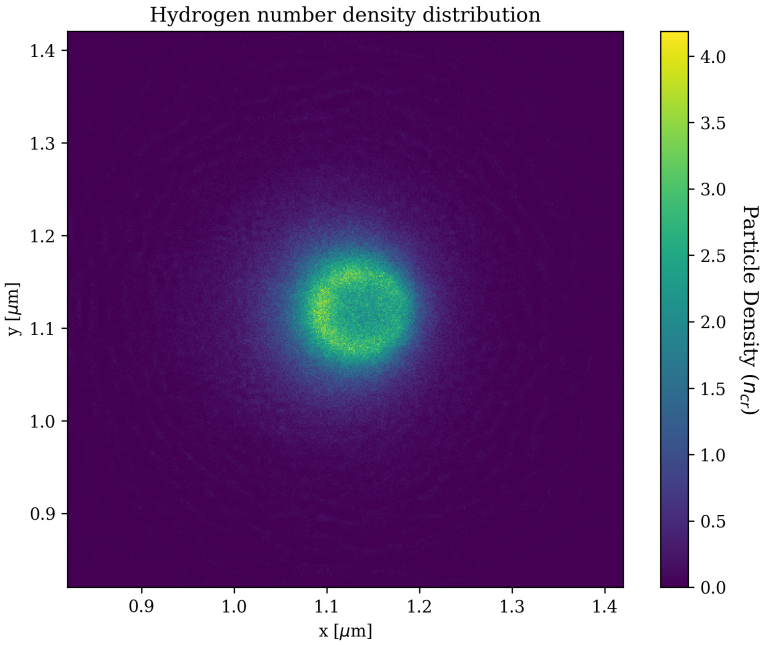

Figure 4.6: 2D distribution of hydrogen number density at 1.0 ps - S-polarization case.

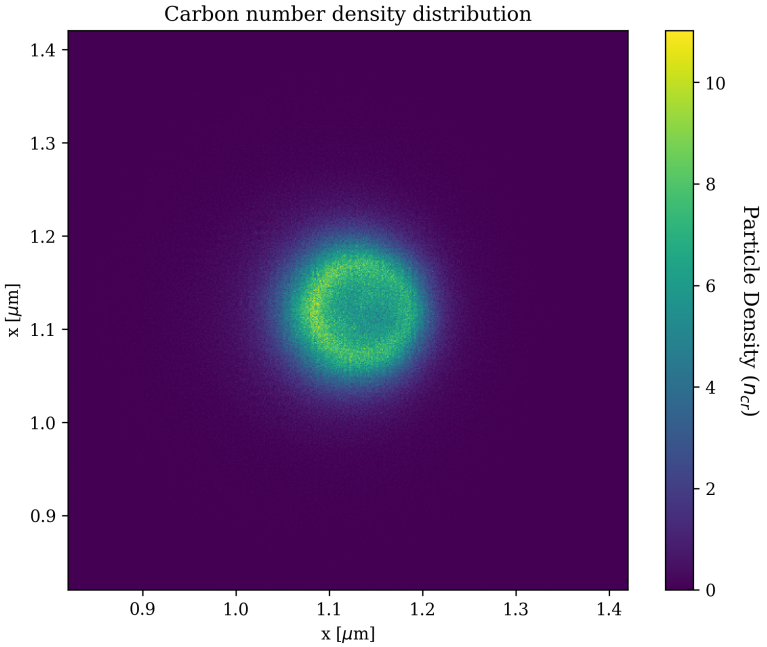

Figure 4.7: 2D distribution of carbon number density at 1.0 ps - S-polarization case.

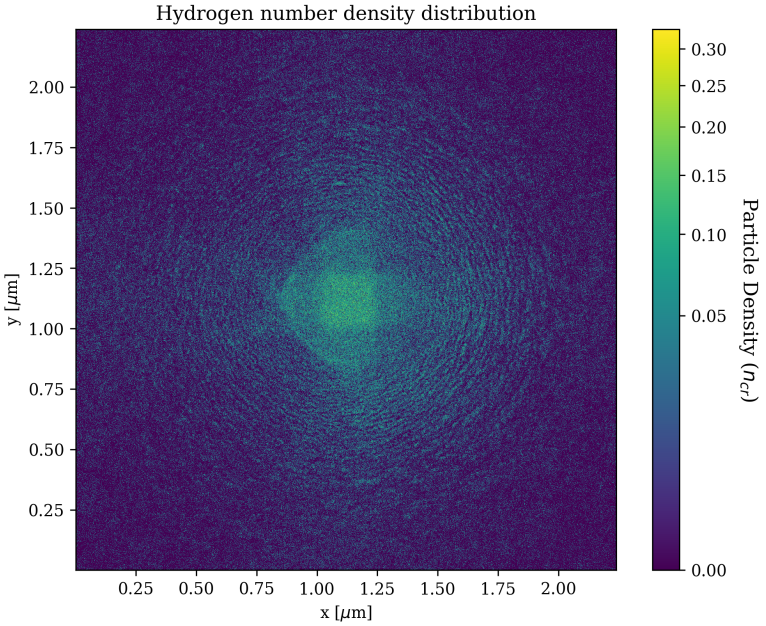

Figure 4.8: 2D distribution of hydrogen number density at 4.0 ps - S-polarization case.

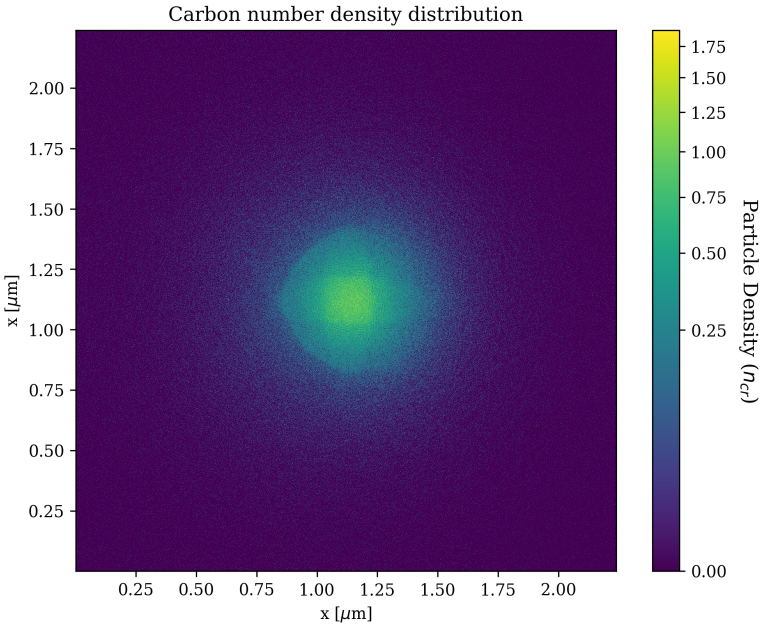

Figure 4.9: 2D distribution of carbon number density at 4.0 ps - S-polarization case.

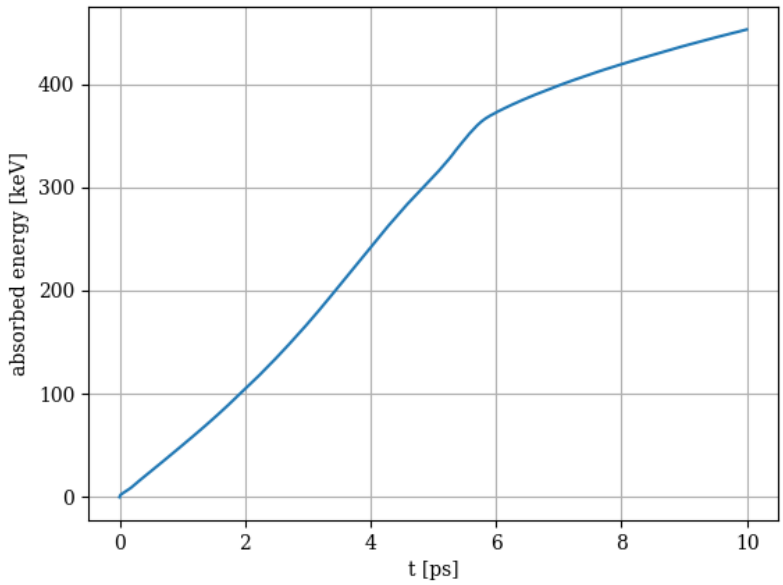

Figure 4.10: Evolution in time of energy absorbed by particles - multispecies, S-polarization case.

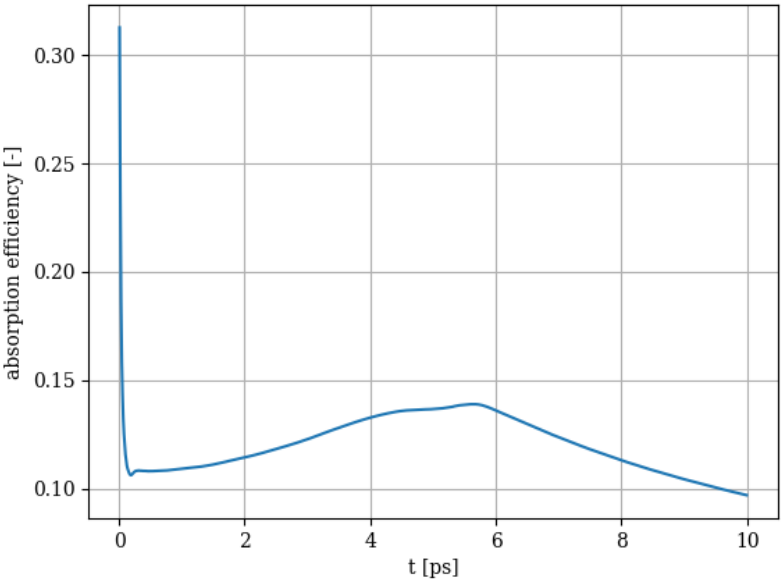

Figure 4.11: Evolution in time of energy absorption efficiency by particles - multispecies, S-polarization case.

4.3 P-polarization

For a P-polarized laser, the density distribution is sensitively different from the averaged case. Charge density distribution is showed in figures 4.12 and 4.13 at times 1.0 ps and 2.7 ps. Here the peak values reached by the electrons density are much lower than the homogenized case; for instance, the peak value during the compression case, at 2.7 ps is almost 90 times the critical density, whereas in figure 3.3 it was just below $110 n_{cr}$.

As far as the energy distribution is concerned, the electron peak density on the left side is slightly lower than the averaged case,0.10 and 0.14 keV at 0.8 and 3.0 ps, respectively, against around 0.11 and 0.16 keV. Instead, on the right side the peak drops much more significantly: for instance, at 3.0 ps it drops from 0.11 to 0.07 keV. An increase in the asymmetry in the distribution between the two sides is observed also for the ions, as showed in pictures 4.15 and 4.16.

As for the energy absorption, the presence of light ions has a smaller impact than it had for the S-polarization. However, the lighter mass of protons does improve the transfer from electrons to ions, and therefore a slight increase is observed. The efficiency still remain around 0.05, while the absolute absorbed energy increases of around 20 keV; the underestimation in considering one ion species is therefore around 8%.

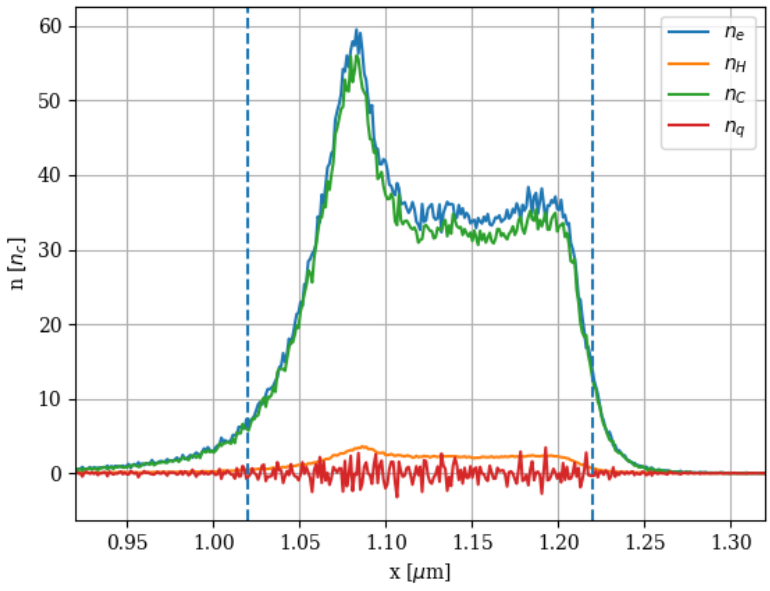

Figure 4.12: Charge density distributions of carbon, hydrogen, electrons and net charge along x at y = $1.1\mu m$, at 1.0 ps - P polarization case

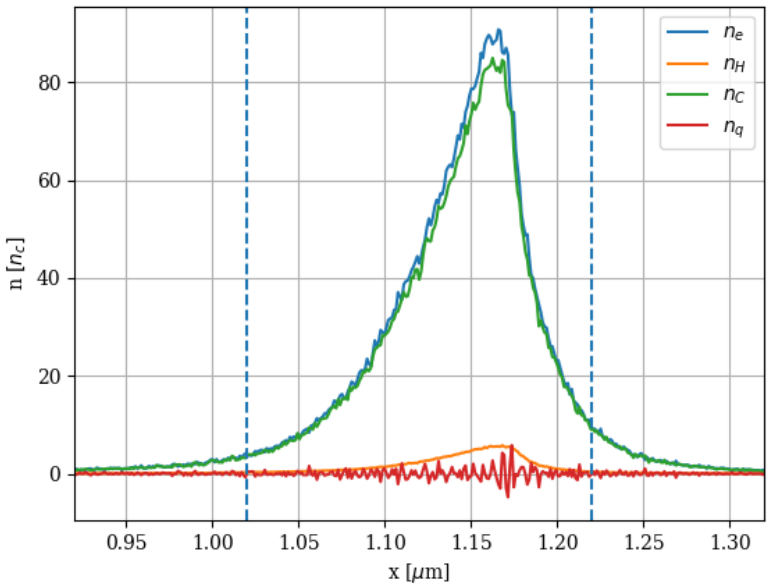

Figure 4.13: Charge density distributions of carbon, hydrogen, electrons and net charge along x at y = $1.1\mu m$, at 2.7 ps - P polarization case

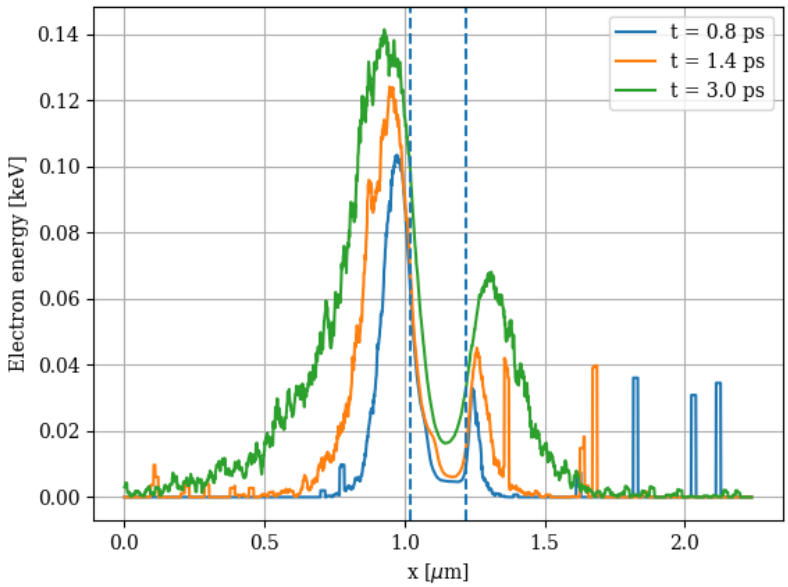

Figure 4.14: Electron energy distribution along x at y = 1.1μm at 0.8, 1.4 and 3.0 ps - multispecies, P-polarization case.

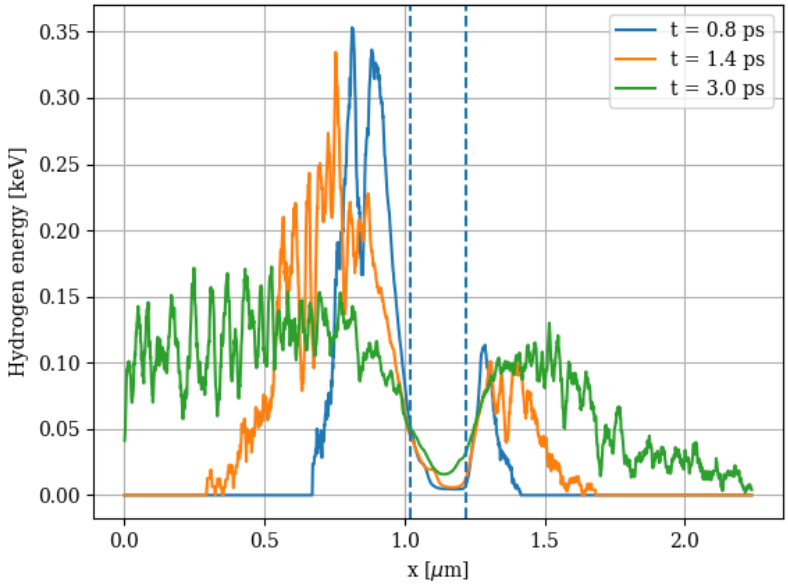

Figure 4.15: Hydrogen energy distribution along x at y = 1.1μm at 0.8, 1.4 and 3.0 ps - multispecies, P-polarization case.

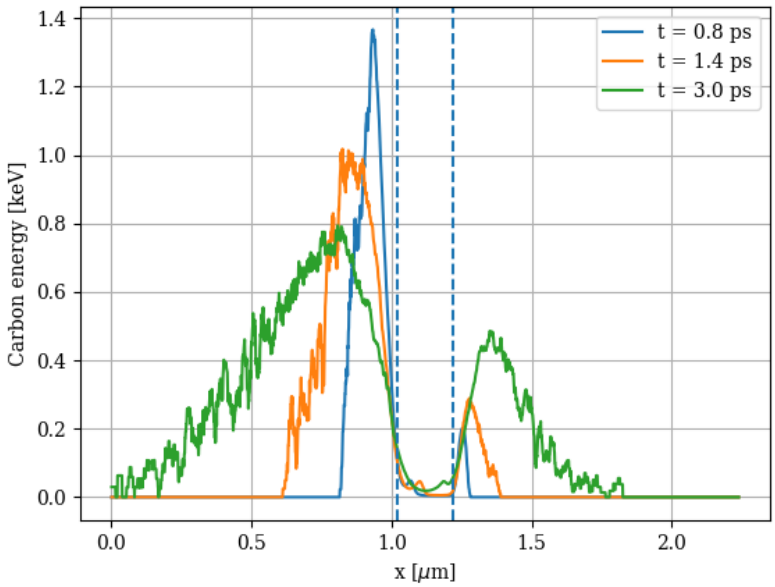

Figure 4.16: Carbon energy distribution along x at y = $1.1\mu m$ at 0.8, 1.4 and 3.0 ps - multispecies, P-polarization case.

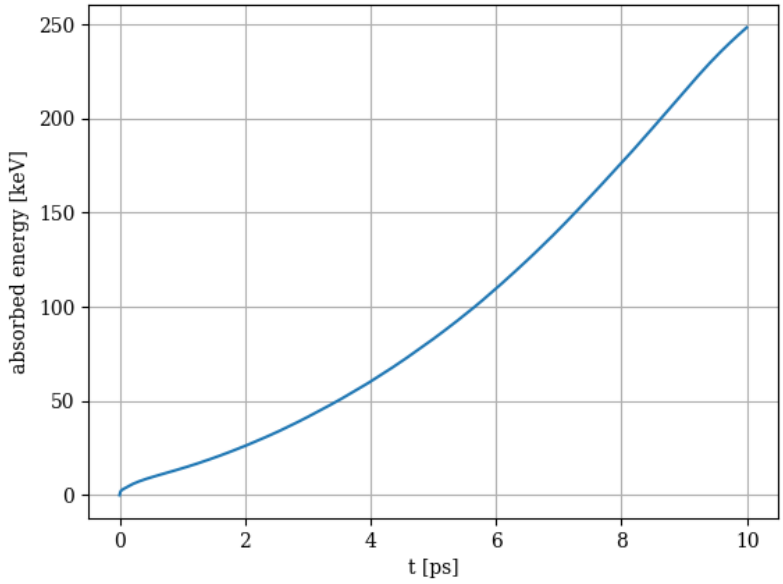

Figure 4.17: Evolution in time of energy absorbed by particles - multispecies, P-polarization case.

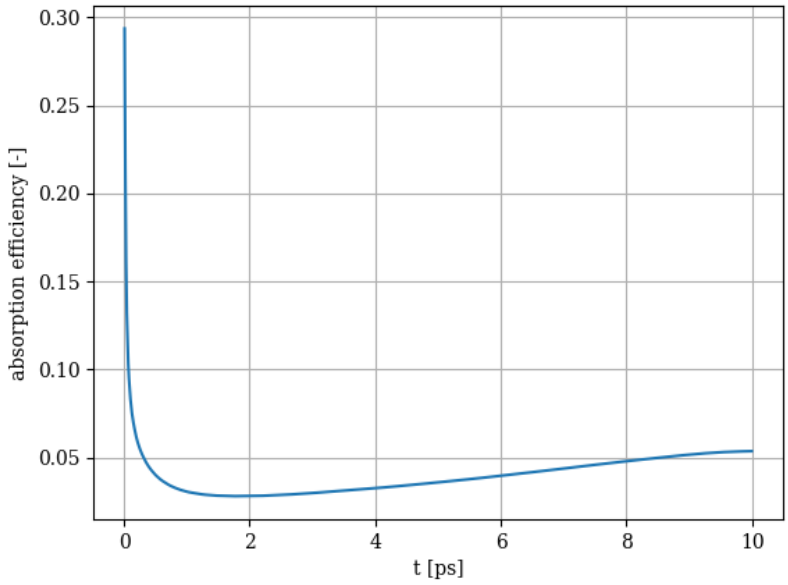

Figure 4.18: Evolution in time of energy absorption efficiency by particles - multispecies, P-polarization case.

Conclusions

The present thesis started by providing fundamentals of plasma physics and then introduced the problem of laser energy absorption by a solid target and possible solution of nano-foams. To asses the influence of some physical parameters, several simulations were run.

The first simulations, differing in the polarization state of a plane wave, showed indeed a different evolution of the plasma target. The S-polarization case exhibited a larger absorption than the other one, both in terms of absolute value of the energy (1.6 times the energy for a P-polarized laser) and double the efficiency. With the aim of maximizing the absorption of the energy carried by the laser, an S-polarization proved to be much more efficient. Furthermore, the evolution time-scales were shorter, and the distributions of density and energy kept a high degree of symmetry. An S-polarized state therefore proves to be a better choice also to produce a homogeneous plasma in shorter time-scales.

A third simulation, again with an S-polarization state, considered a target whose diameter was larger than the laser wavelength. The comparison of the results for two different values of radius highlighted the effect of having a sub-wavelength target. Compression and expansion significantly slowed down, and absorption on the two sides of the cylinder was less uniform. As for the absorption efficiency, accounting for the larger geometry cross-section, a rough estimation yields a result comparable to the sub-wavelength case-

The final chapter was devoted to highlighting the effects of considering two separate ion species, with different charge-to-mass ratio, namely hydrogen and carbon ions, maintaining the same averaged ion properties. The effects of assuming this alternative composition were different for the two polarization states. For the S-case, the two species were impacted to different degrees by the sheath acceleration, leading to the formation of two fronts of expansion for the two ions species. The energy absorption mechanisms were more effective thanks to the presence of lighter ions, allowing an enhancement of the absolute absorbed energy by around 10% and an increase in the energy efficiency from 10 to 12%. For the P-case, instead, the efficiency was almost the same; the main differences lied in the evolution of the target, which was compressed to lower peak densities and exhibited a larger

asymmetry in density and energy distributions. Overall, the results demonstrate that neglecting the difference in the ion species leads to different results concerning the evolution of the target, the ablation process and the homogenization. However, this more precise analysis confirms a better performance for an S-polarized laser in terms of absorption of energy.

Bibliography

[1] P. Gibbon. «Introduction to Plasma Physics». In: *CERN Yellow Report CERN-2016-001* (2014) (cit. on p. 1).

[2] Francis F. Chen. *Introduction to Plasma Physics and Controlled Fusion*. Springer, 2016 (cit. on pp. 2, 6, 12).

[3] Jeffrey P. Freidberg. *Plasma Physics and Fusion Energy*. Cambridge University Press, 2007 (cit. on pp. 2–4).

[4] T.J. M. Boyd and J. J. Sanderson. *The Physics of Plasmas*. Cambridge University Press, 2003 (cit. on p. 4).

[5] H. Conrads and M. Schmidt. «Plasma generation and plasma sources». In: *Plasma Sources Science and Technology* (2000) (cit. on p. 4).

[6] F. Bisti, I. Alexeev, M. Lanzetta, and M. Schmidt. «A simple laser beam characterization apparatus based on imaging». In: *Journal of Applied Research and Technology* (2021) (cit. on p. 5).

[7] L. V. Keldysh. «Ionization in the field of a strong electromagnetic wave». In: *Soviet Physics Jept* (1965) (cit. on p. 5).

[8] Jiguo Wang, Zhenning Guo, Yiqi Fang, Xiaoyang Yu, and Yunquan Liu. «Over-barrier ionization of hydrogen atom in intense circular and elliptical laser fields». In: *Frontiers in Physcis* (2022) (cit. on p. 5).

[9] N. B. Delone and V. P. Krainov. «Tunneling and barrier-suppression ionization of atoms and ions in a laser radiation field». In: *Phys.-Usp* (1998) (cit. on p. 6).

[10] Yaoxing Wu, Girik Jain, Tatyana Sizyuk, Xinbing Wang, and Ahmed Hassanein. «Dynamics of laser produced plasma from foam targets for future nanolithography devices and X-ray sources». In: *Sci Rep.* (2011) (cit. on p. 7).

[11] Alessandro Maffini1 et al. «Nanofoam in action: a versatile tool for laser-plasma interaction experiments». In: *Plasma Physics and Controlled Fusion* (2026) (cit. on p. 7).

[12] Luca Fedeli, Arianna Formenti, Lorenzo Cialfi, Andrea Pazzaglia, and Matteo Passoni. «Ultra-intense laser interaction with nanostructured near-critical plasmas». In: *Scientific Reports* (2018) (cit. on p. 7).

[13] Martina Salvadori et al. «Laser Irradiated Foam Targets: Absorption and Radiative Properties». In: *EPJ Web of Conferences* (2017) (cit. on pp. 7, 43).

[14] Yuriy A. Akimov. «Mie scattering theory: A review of physical features and limitations». In: *physics.optics* (2024) (cit. on p. 8).

[15] H.C. van de Hulst. *Light Scattering by Small Prticles*. Dover Publications, 1957 (cit. on p. 8).

[16] S. Shekhanov, D. Blackman, A. Gintrand, L. Hudec, R. Liska, J. Limpouch, S. Weber, and V. Tikhonchuk1. «Kinetic modeling of laser absorption in foams». In: *Physics of Plasmas* (2025) (cit. on pp. 11, 21, 26).

[17] A. Pukhov. «Particle-In-Cell Codes for Plasma-based Particle Acceleration». In: *CERN Yellow Reports* (2014) (cit. on pp. 13, 15).

[18] T. Zh. Esirkepov. «Exact charge conservation scheme for Particle-in-Cell simulation with an arbitrary form-factor». In: *Computer Physics Communications* (2000) (cit. on p. 16).

[19] J. Derouillat et al. «Smilei: A collaborative, open-source, multi-purpose particle-in-cell code for plasma simulation». In: *Computer Physics Communications* (2017) (cit. on p. 17).

[20] K. Nanbu. «Theory of cumulative small-angle collisions in plasmas». In: *Physical Review E* (1997) (cit. on p. 19).

[21] Andrea Macchi, Marco Borghesi, and Matteo Passoni. «Ion acceleration by superintense laser-plasma interaction». In: *Arxiv* (2024) (cit. on pp. 25, 26).

[22] F. Brunel. «Not-So-Resonant, Resonant Absorption». In: *Physics Review Letters* (1985) (cit. on p. 25).

[23] M. Roth and M. Schollmeier. «Ion Acceleration—Target Normal Sheath Acceleration». In: *Arxiv* (2017) (cit. on p. 26).

[24] Shalom Eliezer, Noaz Nissim, Shirly Vinikman Pinhasi, Erez Raicher, and José Maria Martinez Val. «Ultrafast ignition with relativistic shock waves induced by high power lasers». In: *Arxiv* (2014) (cit. on p. 26).